Crystallisation Characteristics and Crystal Phase Quantification of a Synthetic Lignite Gasifier Slag System

Jan Peter Schupsky[1*], Guixuan Wu[1,2], Muxing Guo[3], Michael Müller[1]

[1] Institute of Energy- and Climate Research – IEK 2, Forschungszentrum Jülich GmbH, Wilhelm-Johnen-Straße, 52428 Jülich, Germany

[2] GTT Technologies, 52134 Herzogenrath, Germany

[3] Department of Materials Engineering, KU Leuven, 3001 Leuven, Belgium

Abstract

The scope of this study is to investigate the crystallisation phenomenon of a synthetic SiO_2-Al_2O_3-CaO-Fe_2O_3-MgO slag system. Firstly, the crystallised phases were predicted by thermodynamic equilibrium calculations. Subsequently, quenching experiments and confocal laser scanning microscope (CLSM) investigations were performed to validate the crystallisation characteristics of the synthetic slag system. Crystallisation kinetics was examined by isothermal quenching and continuous cooling CLSM experiments. The generated samples were analysed by microscopy, XRD, and SEM to determine the crystallised phases by their structure and chemical composition. A detailed insight of the evolution of crystal morphology growth was given. The shape of the two dominant phases: melilite and olivine were described and three-dimensional morphologies were defined for both phases. Additionally, the morphologies were quantified by length and aspect ratio measurements of individual crystals. The morphological information of the olivine and melilite phase, provided in this study, can be used as datasets for a viscosity model for partially crystallised slags. A conceptual viscosity model to be implemented in the next paper of this series, using specialised crystal morphology datasets, can serve a major contribution to forecast slag behaviour and to support the stability of industrial gasifier operation.

Keywords: Entrained flow gasification; coal slag; crystallisation; crystal morphology; viscosity modelling; quenching experiment

* Corresponding author

1 Introduction

Gasification of fuels is a key technology in the modern energy supply market. Gasification technology benefits from the global aim to reduce CO_2 emissions. Due to the higher process efficiency compared to coal power plants and the use of biomass as a fuel, gasifiers have a high flexibility and lower CO_2 emissions. Gasifiers enable short start up and shut down phases, hence gasification can stabilise power grids during renewable energy supply fluctuations [1, 2]. To further increase the efficiency of this bridge building technology, research was done in several fields including i.e. facility design [3, 4], convertible fuels [5, 6] and slag behaviour [7-13]. Especially the slag properties are crucial parameters for the gasification process stability.

During the high gasification temperatures of up to 1600 °C [14] , inorganic compounds of fuel are not converted and are in a liquid state. This so-called slag is present on the refractory walls of the gasifier, constantly flowing downwards that requires suitable flow behaviour. However, with increasing slag viscosity, slag is accumulated on the refractory walls and further agglomeration can lead to a slag tapping blockage. Removing this blockage requires a shutdown of the gasifier and requires additional maintenance time. To ensure an efficient gasifier operation, a deep understanding of the slag properties is required.

Slag viscosity is a commonly investigated property when it comes to describe the slag fluid behaviour. Viscosity is very sensitive to the applied temperature [8]. As the temperature declines, the viscosity of liquids increases. Additionally, slag viscosity can be significantly increased by the phenomena of crystallisation [7, 11, 15]. An increase in viscosity due to solid crystal particles is strongly influenced by the crystal content and the crystal morphology [7, 16]. A brief overview of recent studies, investigating coal slag crystallisation, is given in Tab. 1. The studies were firstly compared, based on the chosen samples. Secondly, the crystallised phases, as predicted by equilibrium calculations, were listed, followed by the experimentally determined crystal phases. By condensing all solid solutions together as one main phase, thermodynamic calculations indicated the presence of 13 phases. However,

61 during the performed experiments, only six different crystal phases were observed in
62 the slag samples (Tab. 1). Furthermore, anorthite and melilite seem to be preferred
63 crystallising phases in the analysed slag systems. It can be concluded that firstly,
64 experimental studies that are more application-related, indicate a fewer number of
65 crystallised phases. Secondly, slag investigations can be performed by focusing on the
66 crystallised phases since there is only a limited number relevant for real gasifier
67 applications. Furthermore, slag systems can be categorised based on their individual
68 crystallisation products and overall conclusions on crystallisation can be made
69 independently of the individual chemical composition of the slag system.

70 **Table 1: Overview of the investigated crystal bearing slag systems by different authors.**
71 **Crystal phases that are also covered in this study are underlined.**

Author	Coal sample	Calculated crystal phases (FactSage)	Investigated crystal phases
Kong et al., 2014 [17]	YL (Yinli) GP (Gaoping) 50/50 blending	mullite, anorthite, cordierite, quartz, clinopyroxene	anorthite
Schwitalla et al., 2017 [15]	slag 3	melilite (>1300°C)	melilite (>1300°C)
Shen et al., 2016 [18]	chinese bituminous coal	hematite, anorthite andradite, gehlenite (melilite), melilite	gehlenite (melilite)
Xuan et al., 2017 [19]	synthetic slag #5	spinel, melilite, merwinite, Ca_2SiO_4	åkermanite (melilite), Mg-Fe-spinel, merwinite
Yuan et al., 2012 [20]	Shenfu	anorthite, wollastonite, gehlenite (melilite), melilite, Fe-spinel, wustite	anorthite, wollastonite, iron silicon oxide
Ren et al., 2018 [21]	BF slag with fly ash F - 2	melilite, anorthite, clinopyroxene, spinel	åkermanite, gehlenite (melilite), clinopyroxene, anorthite

72

73 In this study, crystallisation processes, kinetics and the morphology of crystallised
74 phases of a synthetic oxidic gasifier slag were comprehensively investigated. The
75 analysed slag system consists of five oxidic components, i.e. SiO_2, Al_2O_3, CaO, Fe_2O_3
76 and MgO. Its composition derived from a Rhenish lignite coal ash named HKR that
77 was initially analysed in previous works [22-24].

Initially, equilibrium calculations were performed using FactSage software package and the GTox database for the determination of the liquidus and solidus temperature and the crystallised phases. As a first experimental approach, crystallisation products were investigated throughout a quenching experiment. In a supercooling regime, samples were annealed isothermally and quenched. Subsequently, samples were prepared and firstly analysed via optical microscopy to identify the crystallised samples. Afterwards, crystallised slag samples were analysed via XRD and SEM. Experimental results on the crystallisation characteristics were compared with FactSage predictions.

Furthermore, crystallisation kinetics was investigated by a CLSM set up. Thereby, incubation time, crystal growth, and crystal morphologies were documented. Based on the beginning and completion of crystallisation, the crystallisation kinetics were presented. Lastly, this study focused on the main crystallised phases, melilite and olivine, to provide universal crystal data that are intended to be applicable for all melilite and olivine bearing slag systems. The crystal growth morphologies of both phases were quantified and compared with natural crystal morphologies to prove their validation.

With consideration of the volume fraction and crystal morphology a modified Einstein-Roscoe model is proposed as a first step, in which an effective volume fraction needs to be derived based on specific crystal morphology of each kind of crystals involved. The model will be implemented in the next paper of this series when the viscosity data are available.

2 Experimental

2.1 Synthetic slag samples

The investigated synthetic slag system HKR is based on a Rhenish lignite coal, analysed in previous work [22, 24, 25] (Table 2). HKR is determined to be a Fe-rich coal, originated from the open pit mine Hambach (Germany). To ensure homogeneous bulk and to prevent sample volatility, a generalisation of its composition was made.

Accordingly, HKR slag composition is represented by a SiO_2-Al_2O_3-CaO-Fe_2O_3-MgO system. The slag was mixed using high purity oxidic reagents (Alfa Aesar, Massachusetts, U.S. and Merck, Darmstadt, Germany). The produced slag was in powdery consistency and blended for 24 h to ensure fully homogeneity. The aforementioned generalisation represents 95 wt-% of the real HKR coal ash compounds. The excluded 5 wt-% were redistributed on the network formers SiO_2 and Al_2O_3 (Tab. 2). Due to higher slag acidity and therefore lower crystallisation kinetics, this decision was made to improve the crystallisation investigations during the experiments.

Table 2: Comparison of normalised HKR ash composition after combustion at 450 °C [22] with synthetic HKR slag used in this study. Both samples were analysed by ICP-OES and subsequently normalised to the oxidic compounds.

		SiO_2	Al_2O_3	CaO	MgO	Fe_2O_3	other
real HKR [22]	wt%	31.7	9.7	28.1	11.3	14.2	5.0
synthetic HKR	wt%	34.8	12.0	27.4	11.4	14.4	-

2.2 Thermodynamic equilibrium calculations

The crystallisation behaviour was firstly investigated by the application of thermochemical equilibrium calculations. For this purpose, Equilib module from FactSage (version 7.2) software package (GTT Technologies, Herzogenrath, Germany) was used [26]. Equilib module executes thermodynamic equilibrium calculations to determine stable phases via Gibbs free energy minimisation. In this study, Equilib module was combined with datasets from the GTox database that includes basic thermodynamic data of oxidic compounds [27]. Equilibrium calculations were executed in the temperature regime 1100-1350 °C. To adjust reducing gasifier conditions, an oxygen partial pressure of $\log(p(O_2)) = -12$ bar was set. Equilib calculations were used as an initial reference prediction for the following experiments. In the end, these thermodynamic results were used again to compare the predicted crystal phase formation with the experimentally determined phases.

2.3 Quenching experiment

The experimental procedures were commenced by a sample pre-treatment. To ensure sample homogeneity, synthetic HKR slag powder was filled in Mo-crucibles and annealed in a high temperature furnace (HTF 18/8, Carbolite Gero GmbH & Co. KG, Neuhausen, Germany). During heat treatment, an Ar/4%H_2 gas atmosphere was adjusted, to create reducing conditions. Furthermore, Ar/4%H_2 gas was also used to prevent the used Mo-crucibles from oxidising and therefore to ensure crucible stability. Subsequently, pre-treated samples were used for investigations on crystallisation kinetics and crystallisation behaviour in a quenching experiment [24].

The experiment was performed in a high temperature furnace (ERO 7/50 S, Prüfer GmbH, Neuss, Germany), equipped with a vertical Al_2O_3 tube. Underneath the Al_2O_3 tube, a water basin was placed to ensure a rapid sample quenching. The samples hung in the vertical tube, by the usage of a customised sample holder. A circular Al_2O_3 foam cover closed the experimental set up from the top. In contrast to other studies [28, 29], the unique sample holder allowed individual quenching of several samples during the experiment. Therefore, the applied quenching technique enabled isothermal investigations of a collection of samples under identical conditions. The quenching procedure was performed under Ar/4%H_2-atmosphere with an applied flow rate of 150 ml/min, to create reducing conditions. In the supercooling regime, several isothermal profiles were conducted to analyse the slag crystallisation. The profiles were set between 1350 °C and 1100 °C in steps of 50 °C with an initial cooling slope of -7 K/min. Holding times were set as 0, 1, 4, 7 and 24 hours. As crystallisation was determined to occur after very short incubation times, holding times were reduced to 0, 10, 30, 60 and 120 minutes for 1200 °C and 1100 °C to increase the time resolution of samples at the stage of initial crystallisation. Subsequently after the experiment, samples were prepared for further analysis. Sample crucibles were embedded into epoxy resin, grinded and polished for SEM analysis. A selection of three representative samples was chosen for XRD analysis to confirm SEM results.

2.4 Confocal laser scanning microscope - CLSM

To increase the time resolution for short-termed incubation time, synthetic HKR slag was additionally investigated with confocal laser scanning microscopy (CLSM). CLSM enables in-situ view on the sample during heat treatment. The high temperature furnace (Model SVF17SP, Lasertec, Yokohama, Japan) contains an oval chamber and is coated with an gold layer [30, 31]. In the chamber, a halogen lamp acts as the heat source emitting heat radiation that is focused at the upper part due to the oval shape of the furnace chamber. Because of the halogen lamp, high heating and cooling rates of up to 300 K/min can be applied, compared to conventional furnaces with SiC heating elements. At the focus point, the sample holder and thermocouple are placed and the maximum temperature of 1500 °C can be achieved [25]. The furnace is sealed with a sapphire window containing flange to enable the sample observation. On top of the furnace, the confocal laser scanning microscope (Model 1LM21H, Lasertec, Yokohama, Japan), equipped with a He-Ne laser (wavelength 632.8 nm), was installed [30]. Reducing conditions were applied using Ar gas and a Mg containing furnace, to capture oxygen impurities from the Ar gas. Oxygen partial pressures of less than $\log(p(O_2)) = -12$ bar could be achieved to prevent Mo crucibles from oxidising and to create reducing gasifier like conditions. The oxygen partial pressure was monitored by an oxygen sensor (rapidox 2100, Cambridge Sensotec, St. Ives, Great Britain). The furnace and the microscope were computationally controlled using HiTOS software [31]. Images were taken with magnifications of up to x200 and a frame rate of 1/s.

2.5 Sample analysis

Subsequently after the quenching experiment, Mo crucibles with the slag samples were prepared for SEM-EDX and XRD analysis. To distinguish fully amorphous from partial crystallised samples, initial analysis was conducted via optical microscopy. Therefore, a KEYENCE VHX-S550E digital microscope (KEYENCE DEUTSCHLAND GmbH, Neu-Isenburg, Germany) was used. XRD analysis using a Panalytical EXMPYREAN (Malvern Panalytical, Almelo, Netherlands) device was applied on grinded sample powder from the quenched samples. The XRD

194 measurements were performed, using a Cu Ka anode (40 kV and 40 mA). The SEM
195 and SEMD-EDX analysis were performed by Zeiss Merlin II and Supra 50 VP (Carl
196 Zeiss Microscopy GmbH, Jena, Germany) devices. Also, a selection of CLSM
197 samples was investigated via SEM-EDX analysis. Crystallised phases were
198 characterised by SEM images, EDX point measurements and element mappings, as
199 seen in the chapters 3.3 and 3.4. The results from XRD and SEM-EDX analysis were
200 compared to identify the containing crystal phases. Crystal chemistry and morphology
201 of quenching and CLSM samples were compared to validate the comparability of both
202 experimental approaches.
203

204 # 3 Results and discussion

205 ## 3.1 Modelling partially crystalline slags

206 The viscosity of partially crystalline slags is contributed from two parts: the viscosity
207 of remaining liquid slag (η_l) and the relative viscosity (η_r), due to the crystallised
208 phases. A flowsheet is proposed to determine the viscosity of partially crystalline
209 slags, as shown in Fig. 16. The first part is sufficiently calculated, using a structure-
210 based viscosity model [9, 10, 32, 33]. It was recently developed for molten fuel slags
211 and is described by the function of temperature and the slag composition. In contrast,
212 the second part is much more complex, which is not only related to the volume
213 fraction of crystallised phases, but also to the crystal morphology, the crystal size and
214 the crystal size distribution. Furthermore, the shear rate is also taken into account, if
215 the volume fraction of crystallised phases reaches a critical value that causes the
216 transition from Newtonian to Non-Newtonian fluid behaviour. Therefore, the simple
217 correlation, of the relative viscosity only with the volume fraction of crystallised
218 phases, fails. However, it remains an ongoing challenge to consider all aforementioned
219 parameters influencing the relative viscosity. There are numerous existing viscosity
220 models for suspension systems, such as the Einstein-Roscoe model [34] and the
221 Krieger-Dougherty model [35]. In this study, a modified Einstein-Roscoe model is
222 proposed as a first step with consideration of the volume fraction and crystal

morphology. The volume fraction in the original Einstein-Roscoe model is replaced by an effective volume fraction (see Eq. 1). The contribution of each kind of crystals to the relative viscosity varies, due to different crystal morphologies. Because of that, the quantitative description of the crystal morphology, especially for major crystallised phases, is performed in the previous chapters. The volume fraction of each crystallised phase is calculated from the corresponding mass fraction, predicted by FactSage using GTox database considering their individual crystal morphology. This calculation requires density models for both crystals and remaining liquid slag. Sometimes, the volume fraction is directly estimated by the mass fraction, if the required density models lack. It is noted that the influence of crystallisation kinetics on the volume fraction of crystallised phases is ignored in this flowsheet, which needs to be further considered in the future.

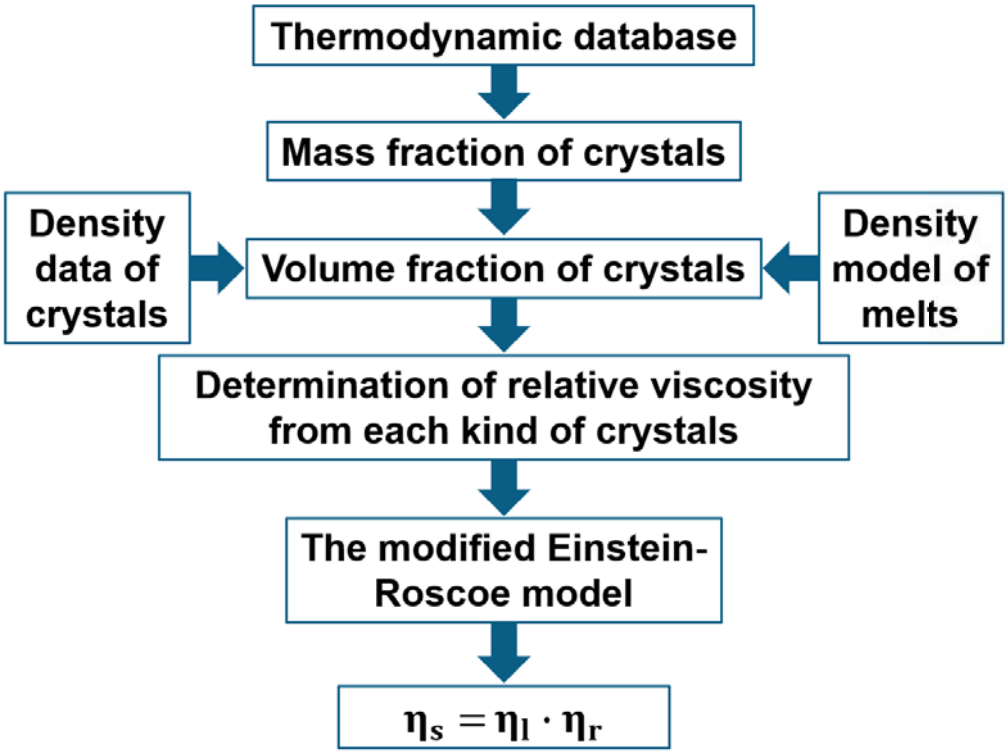

Fig. 1: The flowsheet to modelling the viscosity of partial crystalline slags

$$\eta_r = (1 - \sum_i \alpha_i \cdot V_i)^{-2.5} \quad (1)$$

where V_i is the volume fraction of crystallised phase i; α_i is the weighting factor to determining the contribution of the crystallised phase i to the relative viscosity. The factor α_i is strongly dependent on the aspect ratio and increases generally with increasing aspect ratio.

3.2 Phase predictions via thermochemical calculations

Firstly, to investigate the crystallization processes, thermochemical calculations have been executed to predict the crystallised phases. The FactSage Equilib predictions for the crystallisation of synthetic HKR system are displayed in Fig. 1. Below the liquidus temperature, melilite is the first phase to precipitate. Furthermore, Equilib predicts that melilite miscibility is dominated by åkermanite at temperatures above 1250 °C and dominated by gehlenite at temperatures below 1200 °C. Its overall content fluctuates between 18 and 30 weight percent. The second phase to precipitate is supposed to be olivine, starting at 1290 °C. The olivine content is increasing as the temperature declines, reaching a maximum content of approx. 60 wt-% when the slag crystallised completely at 1130 °C. Olivine mainly consists of kirschsteinit ($CaFeSiO_4$) and monticellite ($CaMgSiO_4$). The spinel phase is dominated by hercynite and spinel. Spinel phase was present between 1260 and 1150 °C and has the least content of all phases in the slag system. At temperatures below 1150 °C anorthite is also supposed to form, reaching a maximum content of 18 weight percent in the HKR slag system. The solidus is reached at 1130 °C. The presence of melilite and spinel in the investigated slag system aligns well with the crystallisation products of aforementioned studies (Table 1, [15, 19, 20, 36]).

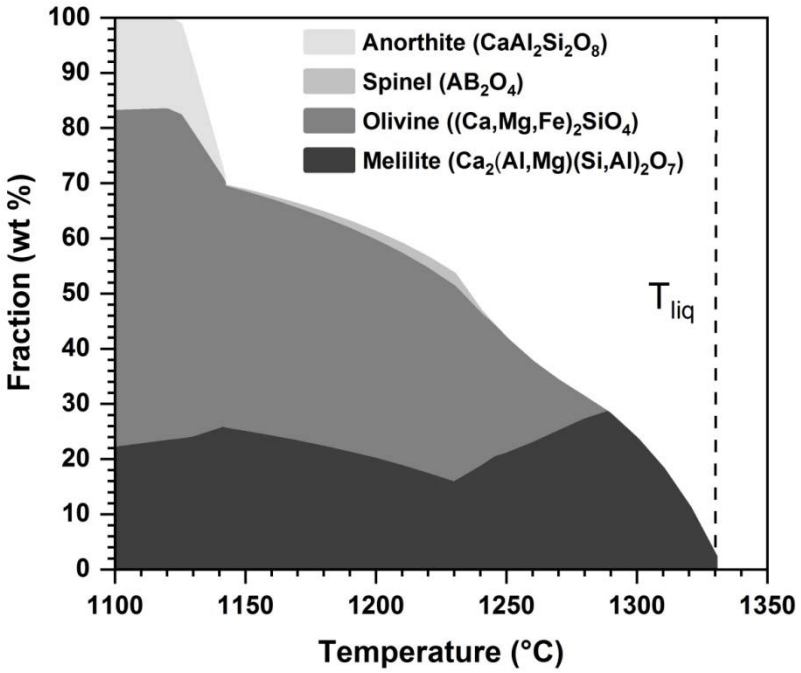

Fig. 2: FactSage Equilib prediction for synthetic HKR slag system at an oxygen partial pressure of $p(O_2)= 10^{-12}$ bar.

3.3 Crystallisation kinetics

Crystallisation kinetics of synthetic HKR slag were determined, based on the results of the quenching and the CLSM experiments. During the experiment, slag samples were supercooled to distinct temperature levels and hold isothermally to document the evolution of crystallisation. As can be seen in Fig. 3, the slag showed no crystallisation at the highest temperatures of about 1300-1350 °C, though a crystallisation should occur at 1330 °C as seen in the equilibrium calculations (Fig. 1). As the temperature is reduced to at least 1250 °C an expansive crystallisation zone was documented. Crystallisation kinetics were high enough to initiate crystallisation below 1300 °C throughout the cooling slope of -7 K/min. Accordingly, all samples below 1300 °C are expected to be influenced by crystallisation occurring already at higher temperatures. Due to the fact that the crystallisation zone could not be bypassed by a sufficient cooling slope, the zone of glassy solidification below the crystallisation zone could not be accurately determined by this experimental approach.

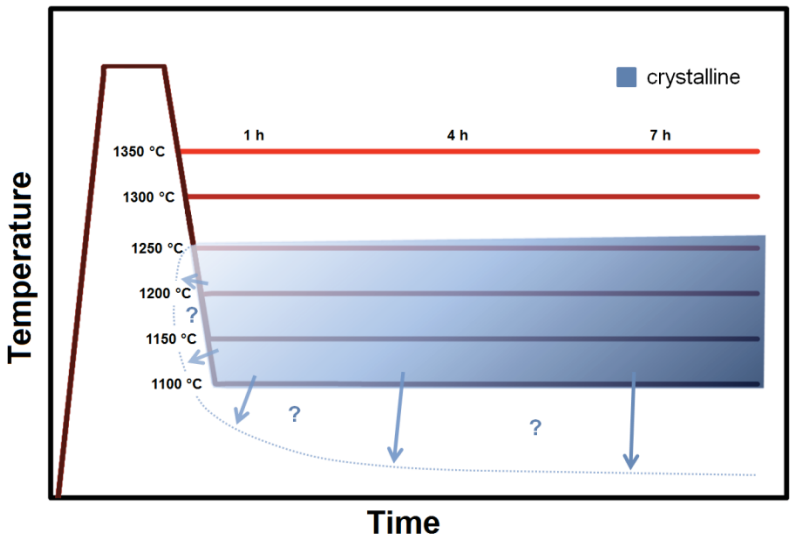

Fig. 3: Time temperature transformation (TTT) diagram of the synthetic HKR slag, based on the quenched samples. The borderlines of the crystallization zone could not be fully determined by the quenched samples as suggested by the dotted line.

CLSM experiments were conducted to document the crystallisation kinetics in more detail and to determine, if a glassy solidification of HKR slag can be achieved. Therefore, measurements with high cooling rates were applied: -7, -15, -30, -60, -100, -150, and -200 K/min. Crystallisation phenomena were observed for each cooling condition as displayed in Fig. 3. The initial crystallisation temperatures were determined at 1270 °C for low cooling rates (-7, -15, and -30 K/min). For the high cooling rates (-100, -150, and -200 K/min), initial crystallisation temperatures are settled at approx. 1150 °C. In contrast, the temperatures at which no further crystallisation progress was observed i.e. completed, are constantly declining from 1150 °C (-7 K/min) to 975 °C (-200 K/min). In between, the average initial crystallisation temperatures and the average temperatures of crystallisation completion was a crystallisation zone defined (Fig. 3). CLSM results further indicated that HKR slag could not be sufficiently supercooled to bypass the crystallisation zone with applicable cooling rates. However, water quenched samples from higher temperatures (e.g. 1300 °C), showed a completely glassy solidification (Fig. 2). Thus, it was concluded that the investigated slag system tended to crystalise even at high cooling rates but solidifies amorphous in the case of an instant quench above 1300 °C. For the case of a gasifier application, the crystallisation tendency of HKR slag in the

downwards flowing slag layer on the refractory walls needs to be considered to prevent an uncontrolled blockage of the slag flow.

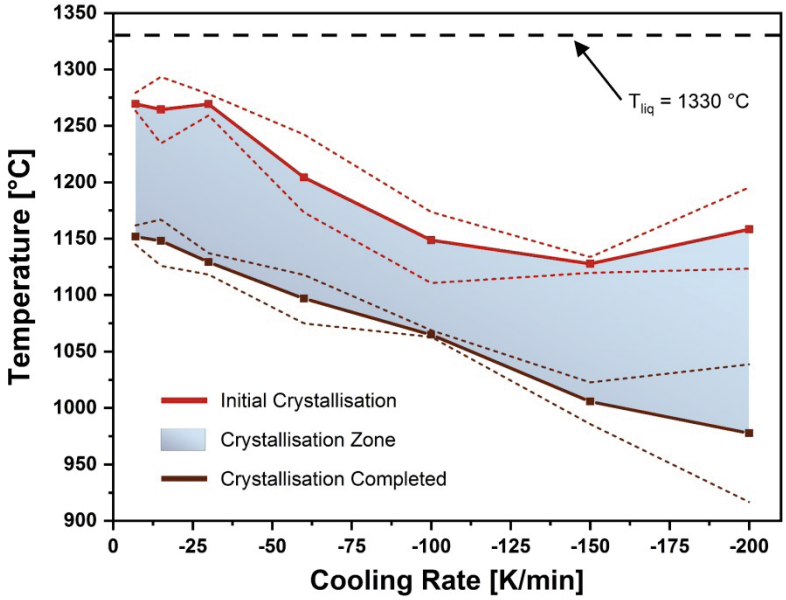

Fig. 4: Synthetic HKR crystallisation zone, defined by the average initial crystallisation temperatures and the average temperatures of crystallisation completion, as determined via CLSM cooling rate experiments. The dotted lines represent the maximum and minimum temperatures for the respective slag crystallisation behaviour. Each slope measurement was repeated three times.

3.4 Crystallised phases of synthetic HKR slag

Crystallisation of HKR slag system was also investigated by samples of the quenching and the CLSM experiments. A total amount of 30 samples were quenched after certain holding times in the supercooling regime. Fig. 4 displays a microscopic view of two representative samples, which experienced the same holding time of one hour at temperatures of 1250 °C and 1150 °C. HKR slag showed a brownish to blackish colour in the Mo crucibles (left column, Fig. 4) and is interspersed with several cracks originated from the quenching procedure. Furthermore, both images indicate rectangular, prismatic macro-crystals with a millimetre scale size that formed in the slag. This three-dimensional view was enabled due to the utilisation of transparent epoxy resin and ring-light observations with the digital microscope. However, the

311 images made by coaxial-light mode reveal divergent symmetries.

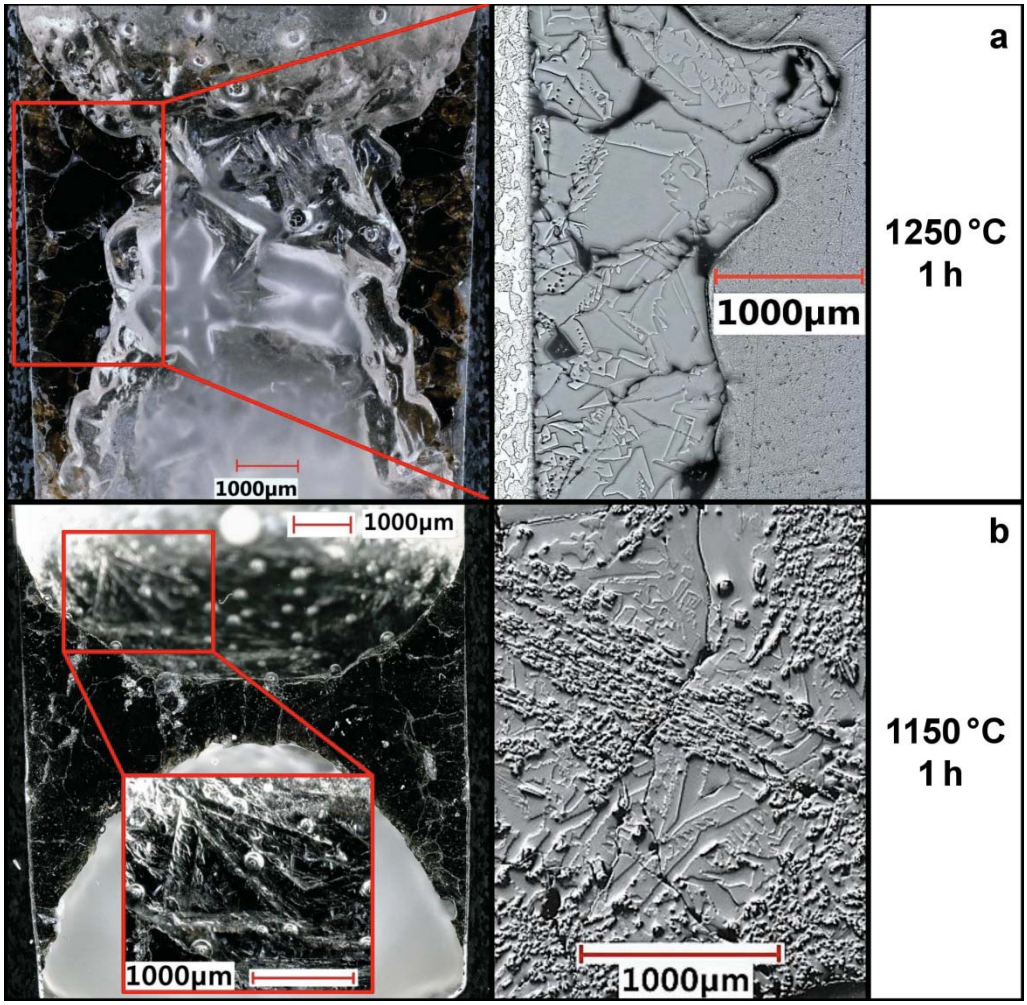

Fig. 5: Microscopic view of two representative samples quenched at 1250 °C and 1150 °C after a holding time of 1 h each. Images in the left column are made by ring-light mode and images in the right column are taken by coaxial-light mode of the used digital microscope.

312

313 At 1250 °C, a selection of macro crystals is present, which are partially in a dendritic
314 or skeletal shape. Additionally, at least one more crystalline phase can be identified,
315 especially in Fig. 4 b (1150 °C). Coaxial-light mode revealed the presence of a smaller
316 granular fraction with spatial distribution that sometimes showed an aligned
317 arrangement. In contrast, at 1250 °C (Fig. 4 a) only very few granular particles could
318 be identified close to the crucible walls. To enhance the understanding of the crystal
319 growth evolution, two samples, investigated by CLSM are displayed in Fig. 5. In-situ
320 imaging indicated the growth of quadrangular crystals, floating on the liquid slag
321 (Fig 5 a). The microscopic image indicates that several quadrangular crystals with
322 sizes up to a millimetre scale were present in the slag after 30 minutes of holding time.

However, as the in-situ CLSM image shows, holding times of 750 s enabled such crystals to grow, already. Fig. 5 b documents that also at approx. 1150 °C (applied cooling rate: -200 K/min) quadrangular crystals formed in the slag. By taking the post-experimental digital microscope image into account, the quadrangular, prismatic crystals can be described further as four-sided pyramids. The overall crystal dimensions and morphologies are of a comparable matter with the morphologies revealed under ring-light mode of quenched samples (Fig. 3, 4).

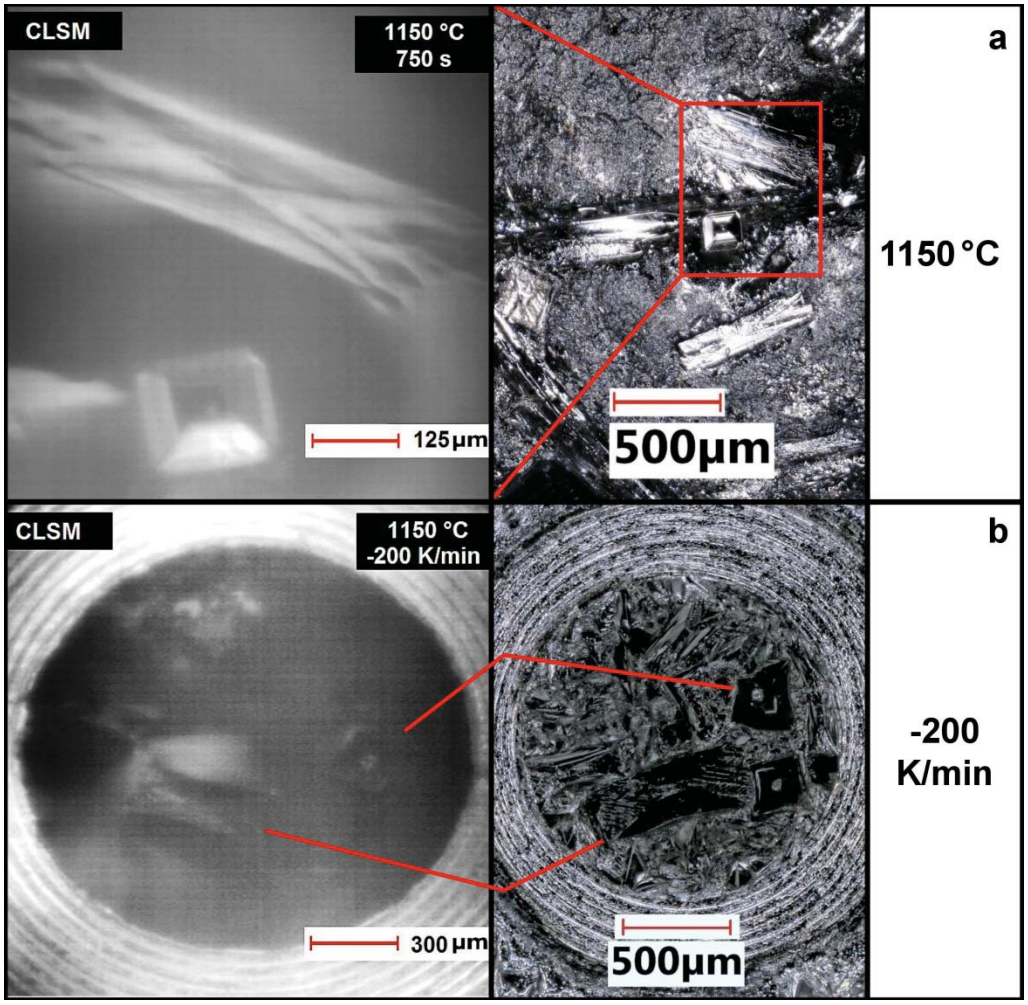

Fig. 6: CLSM in-situ view (left column) and microscopic view (right column) of two representative CLSM samples. Microscopic images were taken with ring-light mode after the experiment. a was supercooled to 1150 °C and hold for 30 minutes, ultimately. b was constantly supercooled with a slope of -200 K/min.

3.4.1 Phase Determination by Crystal Structure

The crystalline content of quenched samples was analysed by XRD regarding to their crystal structure. A selection of three samples was chosen and is displayed in Fig. 6, representing 1250, 1150 and 1100 °C. The holding times of the samples are in a range

of 0 minutes (instant quench) up to 60 minutes. As the comparison of the analysed spectra indicates, all samples are in a very well agreement with each other. Major peaks are present in all samples, also displaying similar peak intensities. However, the sample quenched at 1250 °C contains a slightly higher background signal between 25 and 35 2Θ, which represents the amorphous slag that was still present in the sample. Compared with the instant quenched sample at 1100 °C, the noticeable presence of amorphous slag at 1250 °C (60 min holding time) is an indicator for an overall lower crystallisation content and therefore slower crystallisation kinetics (Fig. 6). Melilite was undoubtedly identified as the main phase in all spectra. Peak positions and also peak intensities are in coincidence with ICSD dataset 187934 for melilite phase (Ca_2 ($Mg_{0.495}$ $Fe_{0.202}$ $Al_{0.303}$) ($Fe_{0.248}$ $Al_{0.216}$) $Si_{1.536}$ O_7). As a second phase, forsterite was identified in the XRD spectra. Though, the overall accordance with ICSD dataset is less plainly, compared with melilite. Quantitative analysis of the XRD spectra indicated degrees of crystallinity for melilite and forsterite of 98:2 (1250 °C), 95:5 (1150 °C) and 83:17 (1100 °C), respectively. Ultimately, it can be concluded that forsterite is preferably crystallising at lower temperatures compared with the melilite phase. The overall crystallinity was determined in the range of 70- 80 wt-%.

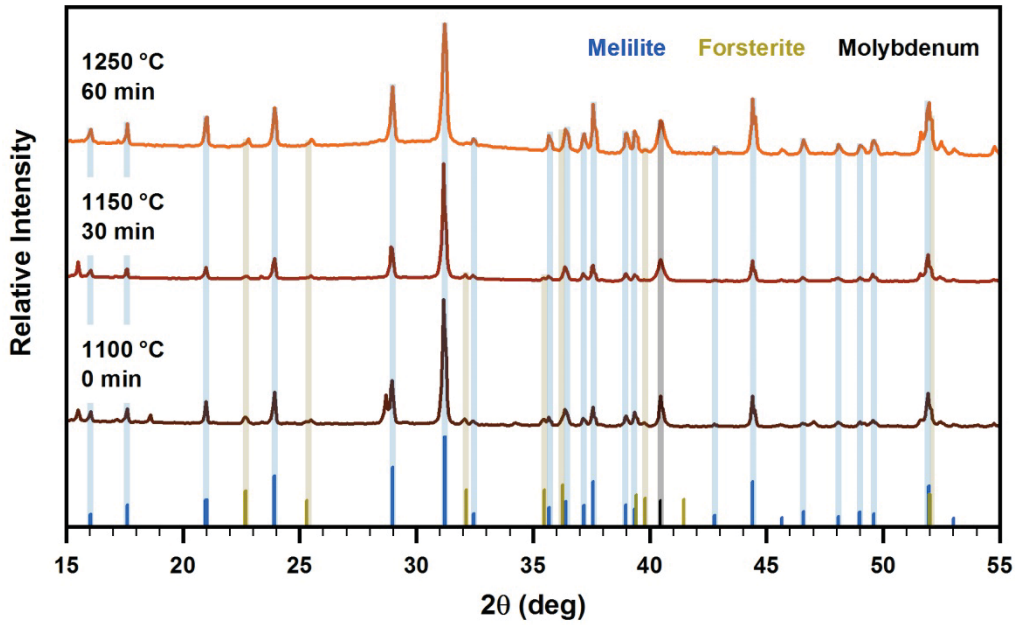

Fig. 7: XRD spectra of three representative samples quenched at 1250, 1150 and 1100 after holding times of 0, 30 and 60 minutes. The correlated datasets are: melilite (blue), forsterite (green) and molybdenum (black). Datasets derive from ICSD database.

3.4.2 Phase determination by chemical composition

The samples treated in the quenching as well as in the CLSM experiments were further analysed by SEM and SEM-EDX analysis. SEM analysis provide a highly detailed view on the structure of the crystallised phases and EDX measurements reveal their chemical composition. A representative sample, quenched at 1250 °C after 4 h of holding time, was chosen to display the crystallised phases: melilite, olivine and spinel (Fig. 7). Those three phases crystallised in distinctly different shapes and sizes. While melilite grew in the form of dendritic to skeletal macro-crystals, olivine crystallised in hyp-, idiomorphic, angular crystals with intermediate lengths of maximum 300 µm. Lastly, a spinel phase with limited crystal sizes and idiomorphic appearance was found as well (Fig. 7 c). Regarding to EDX point measurements of the crystallised phases, melilite composition is in a very good agreement with a melilite solid solution of 75% åkermanite and 25% gehlenite (Fig. 7c,d). Referring to all analysed slag samples, the melilite phase is always dominated by åkermanite with contents between 50% and 85% compared to the corresponding endmember gehlenite. As already described by XRD results (Fig. 6), the amount of olivine crystals is

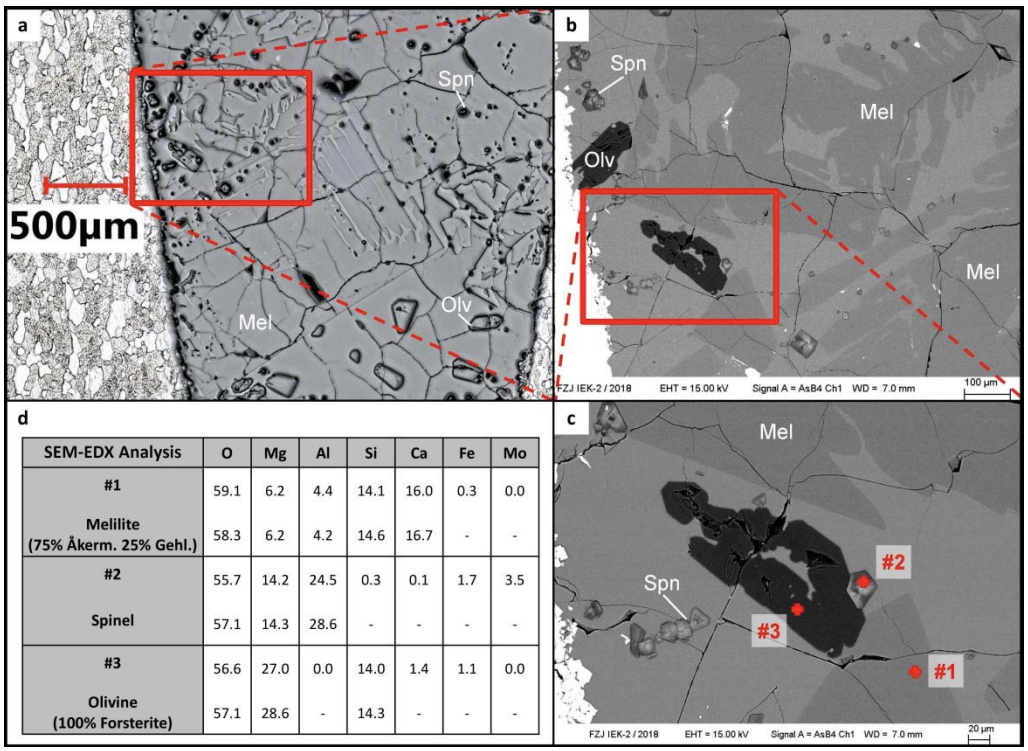

d

SEM-EDX Analysis	O	Mg	Al	Si	Ca	Fe	Mo
#1	59.1	6.2	4.4	14.1	16.0	0.3	0.0
Melilite (75% Åkerm. 25% Gehl.)	58.3	6.2	4.2	14.6	16.7	-	-
#2	55.7	14.2	24.5	0.3	0.1	1.7	3.5
Spinel	57.1	14.3	28.6	-	-	-	-
#3	56.6	27.0	0.0	14.0	1.4	1.1	0.0
Olivine (100% Forsterite)	57.1	28.6	-	14.3	-	-	-

Fig. 8: Representative crystallised phases in a HKR sample, quenched at 1250 °C after 4 hours of holding time. a the microscopic view of the quenched sample. b, c SEM BSE images of the same area as seen in a, including locations of EDX point measurements. d data of the EDX point measurements seen in c, in the unit of atom%.

significantly lower compared to the melilite phase, which is also indicated by the SEM results (Fig. 7b). EDX point measurements reveal that the olivine phase consists almost completely of forsterite, the Mg-rich endmember of olivine. SEM analysis of further samples proved that also fayalite (Fe-rich) and monticellite (Ca-rich) contribute to the olivine phase, nonetheless forsterite remains as the dominant endmember. In contrast to the XRD data, very low portions of $MgAl_2O_4$-spinel (Fig. 7d) were present in several slag samples. The spinel phase also incorporated amounts of iron, resulting in a solid solution of spinel and hercynite. The apparent mismatch between XRD and SEM results concerning the presence of spinel can be explained, regarding to minor amounts of spinel crystals that did not generate enough reflection signals.

The determined crystallised phases were also found in the CLSM samples. An SEM-EDX elemental mapping is shown in Fig. 8 that contained the aforementioned phases as well. CLSM data also indicated that melilite is the major phase in synthetic HKR slag. As melilite has a comparably high content of Ca and shows non-incorporation of

Fe, it can be clearly identified in the mapping (Fig. 8). The already displayed crystal shape of olivine (Fig. 7) can be added by an elongated macro crystal shape (Fig. 8). Regarding to Fig. 8, it needs to be noted that the olivine macro crystal growth was enabled because of the free space in the intercrystalline gap between the melilite crystals. Due to the high content of Mg and the lack of Ca and Al, the olivine phase can be clearly distinguished from the remaining sample (Fig. 8). Ultimately, the

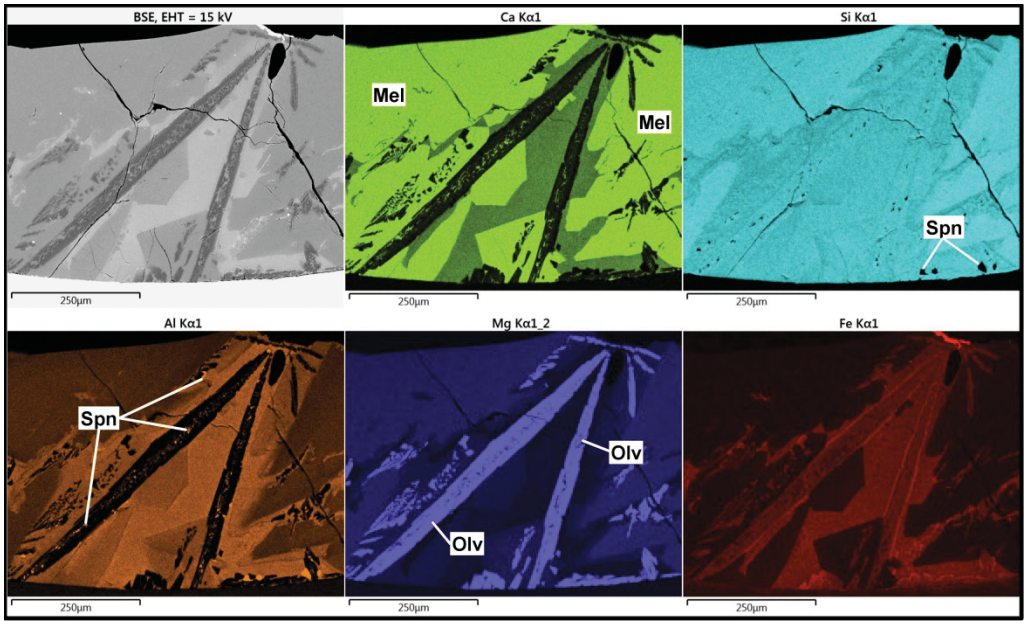

Fig. 9: SEM-EDX elemental mapping of a HKR sample investigated by the CLSM experimental set up. The sample was constantly supercooled with a slope of -6 K/min.

SEM-EDX mappings further revealed that the spinel phase faces a strong association with the olivine phase. Spinel even crystallised in the hollow olivine macro crystal (Fig. 8, Al mapping). The association of crystal phases is not of a random nature, thus it is based on the fluctuations of the slag chemical composition, that is induced by the initial crystallisation. The melilite phase is expected to grow first, based on its dominant portion in the slag and the fact that melilite crystal growth shows principally no sign of growth restriction by other crystal phases. The SEM-EDX data (Figs. 7 and 8) give evidence that melilite formation leads to an enrichment of Fe and a depletion of Ca in the remaining liquid slag, which in turn favors the growth of Mg-, Fe- olivine. Subsequently, olivine formation leads to a signficant enrichment of Al in the slag, as it can not be incorporated by the olivine structure. Eventually, the Al-rich spinel phase grows in a very close arrangement with the olivine crystals.

3.4.3 Comparison of experimental data with equilibrium calculations

To conclude the main results of HKR slag crystallisation behaviour, a comparison of the experimental results with the thermochemical equilibrium calculations is meaningful. In general, it can be summarised that the predicted liquidus temperature of 1330 °C (Fig. 1) could not be confirmed by the quenching or the CLSM experiments (Figs. 2 and 3). Nonetheless, it is arguable that a small degree of supercooling could lead to a metastabile slag state, especially due to the fact that the slag was observed in an overall hour-timeframe that may not allow an equilibrium to form. The predicted crystallised phases however, are in good agreement with the determined phases in the samples (Figs. 1, 6, 7, 8). Melilite and olivine were found in large and noticeable amounts, respectively and traces of spinel were also present. Melilite is the initial crystallising phase, proven by the calculations and the experiment. Thus, the overall distribution is shifted to the favors of melilite (Figs. 7 and 8), while FactSage calculations assumed a dominance of olivine instead. The predicted anorthite phase could not be identified in the samples. Although, all analysed samples contained left-overs of liquid slag, which could have served as a source for further potential crystallisation. Thus, the possibility of anorthite formation after the investigated time horizons can neither be confirmed nor disproved beyond doubt.

3.5 Quantification of dominant crystallised phases - Olivine

Melilite and olivine represent the main crystallising phases in the synthetic HKR slag system. A detailed crystal shape quantification is necessary to generate morphology data that can be used in a viscosity model for partially crystallised slags. As already implied in Fig. 7 and 8, olivine crystallised as micro and as macro crystals. Though both morphologies seem to be incompatible with each other, an overall crystallisation mechanism could be identified in the investigated samples.

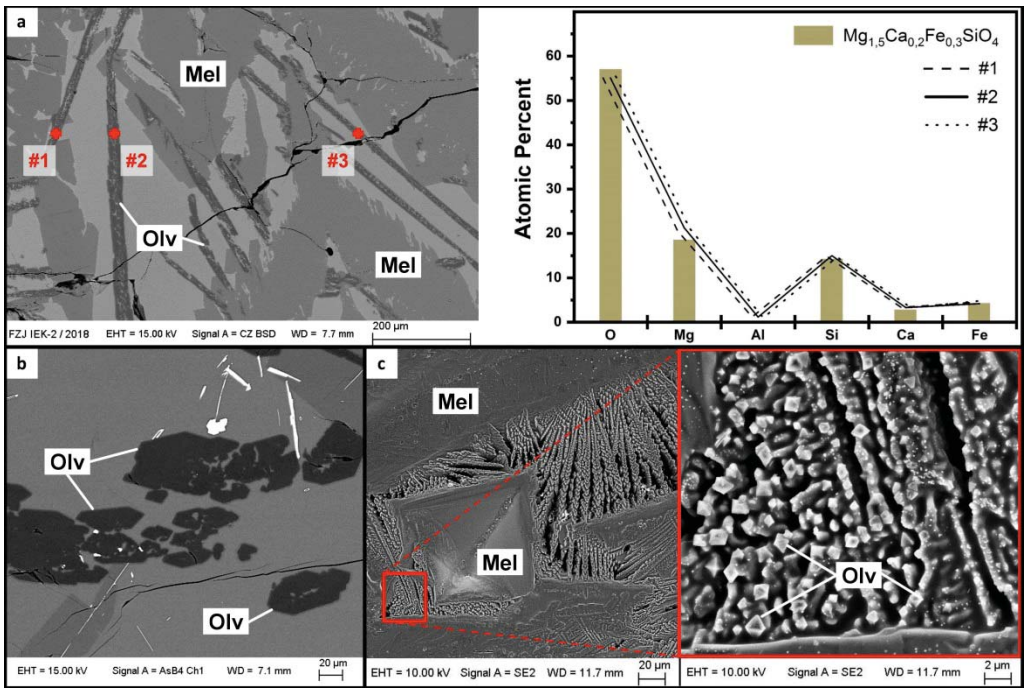

Fig. 10: Representative samples of olivine crystallization of the synthetic HKR slag system. a SEM BSE image of a samples immediately quenched at 1150 °C. Three olivine macro crystals were investigated via EDX measurements and compared with an olivine (Mg-Ca-Fe) solid solution, b SEM BSE image of a sample quenched at 1150 °C after 30 min of holding time, c SEM image of the sample surface, investigated via CLSM and an applied cooling rate of -100 K/min.

As Fig. 9a indicates, the olivine macro crystals were also characterised by SEM analysis. The olivine macro crystals incorporated Ca and Fe, representing a solid solution from forsterite (Mg_2SiO_4), fayalite (Fe_2SiO_4) and monticellite ($Ca,MgSiO_4$). That solid solution composition represents the average olivine composition of all micro and macro crystals quite well. A detailed spatial view on the olivine crystals is displayed in Fig. 9c. Olivine crystals appeared in parallel aligned elongated macro

crystals that consisted of single rhomboid crystals. As shown in Fig. 7b, olivine crystal shapes show a high accordance with an ideal type rhomboid shape. Some crystals appeared to be hollow. Hence it can be concluded that the individual growth was not fully completed as the sample was quenched. Due to the hollow appearance of olivine crystals, it can be assumed that olivine crystallisation did not reach an equilibrium state with slag system.

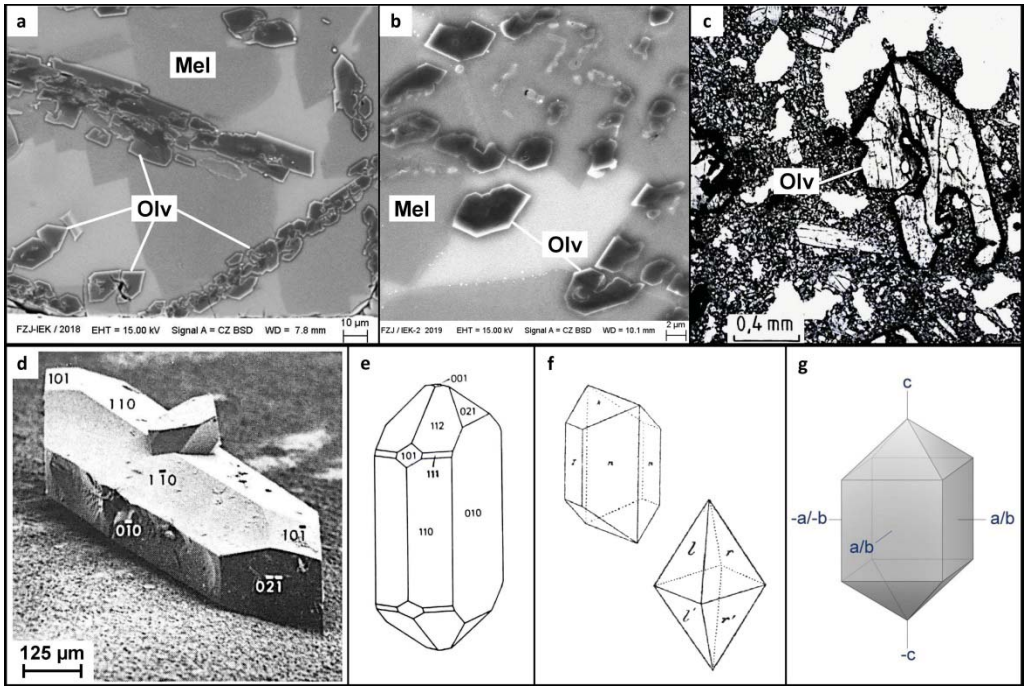

Fig. 11: Comparison of investigated olivine crystals (a,b) with typical olivine morphologies (c-g). CLSM samples crystallised at an applied cooling slope of -6 K/min (a) and at isothermal treatment of 1100 °C (b). Cross section of an alterated hypidiomorphic olivine crystal in an alkaliolivinebasalt, modified after Pichler & Schmitt-Riegraf (1982). d forsterite crystal derived from crystal growth experiment and calculated growth form of an olivine type mineral (Hart, 1971). f early description of olivine crystal morphologies by Goldschmidt (1918). g generalized elongated, equiaxed bipyramidal morphology, generalized for the olivine crystal quantification.

CLSM samples displayed in Fig. 10 a,b give additional evidence of olivine rhomboid crystal shape based on samples cross section analysis. The presence of rhomboid olivine crystals in various samples, investigated in both of the experiments, suggests that the experimental results are absolutely comparable and that olivine shape formation underlies an overall characteristic. Rhomboid olivine crystals are also found

in magmatic rocks, as shown in Fig. 10 c [37]. Compared with the analysed synthetic slag system, it can be stated that olivine crystallisation shape is characteristic and independent of the analysed supercooled liquid system. Based on that conclusion, fundamental findings in the field of mineralogy and crystallography can be used to define a valid spatial morphology of olivine crystals. The typical olivine morphology (Fig. 10 d, e, f) was already described several decades, respectively a century ago [26, 38] and coincides with the results described in this study very well. Accordingly, a single olivine crystal is described as a rhomboid-bipyramid (Fig. 10 f), which is elongated in the direction of the c-axis. To define a three-dimensional morphology, based on the two-dimensional information from the cross sections of samples, generalisations on the crystal morphology were made. Firstly, olivine crystal surface arrangement was defined as an equiaxed rhombic-bipyramid with a variable elongation in the c-axis direction (Fig. 10 g). Secondly, the main morphology was described by the length and the aspect ratio of the bipyramid, determined by length and width measurements of single olivine crystals. Since the bipyramid is defined as

equiaxed, the crystal width is identical with the crystal depth (Fig. 10 g).

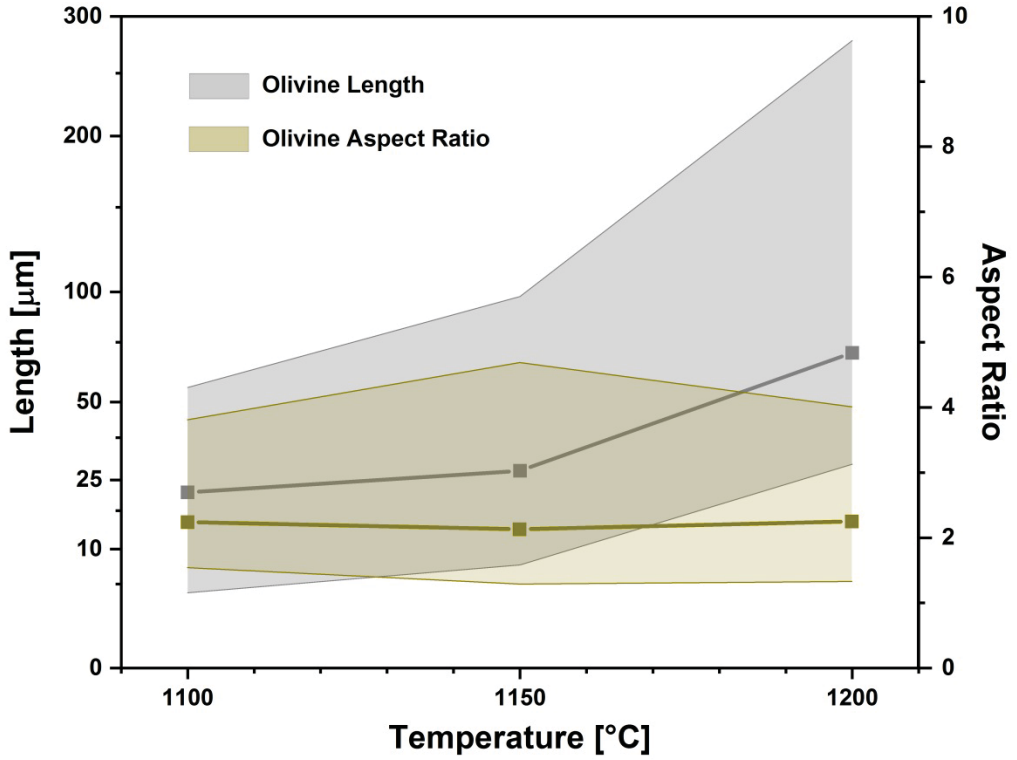

Fig. 12: Olivine crystal morphology quantification based on samples from the quenching and the CLSM experiments. Maximum, minimum, and average crystal length as well as crystal aspect ratio in dependency of the temperature. The x-axis is in logarithmic scale.

Olivine morphology data were quantified (Fig. 11) by the analysis of 119 single crystals in a variety of samples. Samples from both, the quenching and the CLSM experiments were used therefor. As the investigated target temperature is raised, the average olivine crystal length is increasing from 21.8 µm (1100 °C) to 70.2 µm (1200 °C), as well. Concurrently, the range between the maximum and minimum crystal length also increased at higher temperatures. However, olivine crystals with a triple digit micrometre length were seldom, indicated by an overall moderate increase in the average crystal length. The fundamental characteristic of growing larger crystals at higher temperatures is in agreement with the general crystallisation theory [39, 40]. A smaller degree of supercooling (i.e. higher temperatures) led to the growth of few, but larger crystals, as the growth was the dominating driving force. These mechanisms did not impact the overall olivine crystal shape, due to its constant aspect ratio (Fig. 11). Regarding to the fact that data from the two experiments with completely different set ups, including various holding times and sample amounts, were

incorporated in the quantification, it is notable that the crystal aspect ratio subjected only minor fluctuations between 2.13 and 2.25 (1150 °C, 1100 °C). As a consequence, it can be concluded that the experimental approaches served trustworthy and comparable results. Furthermore, it was proved that the generalised rhomboid bipyramid is an absolutely applicable morphology to describe the olivine phase that can be implemented in a viscosity model for partially liquid slags. However, it must be noted that the elongated macro crystal shape of olivine is not represented by the single crystal morphology described above. Its macro dimensions are strongly impacted by the available space in the intercrystalline gaps of the slags crystallised texture.

3.6 Quantification of dominant crystallised phases - Melilite

Melilite is the dominant phase in the synthetic HKR slag system. Therefore, the quantification of its crystal morphology is essential to understand the impact of crystallisation on the viscosity of the HKR system. The melilite phase was identified to form comparable large dendritic, skeletal crystals (Fig. 7). Those crystal morphologies were also displayed in cross sections (Fig. 4), indicating recurring melilite morphology. However, CLSM images of the samples surface (Fig. 5) indicated large crystals with a pyramidal and an hour-glass shape but no dendritic or skeletal crystals. Nonetheless of this apparent discrepancy in the crystal structure, SEM-EDX measurements indicated a uniform melilite solid solution, with dominance of åkermanite in all of the aforementioned morphologies.

Hence, a selection of samples treated in the quenching and the CLSM experiments were chosen to validate the systematic of the melilite morphology (Figs. 12 and 13).

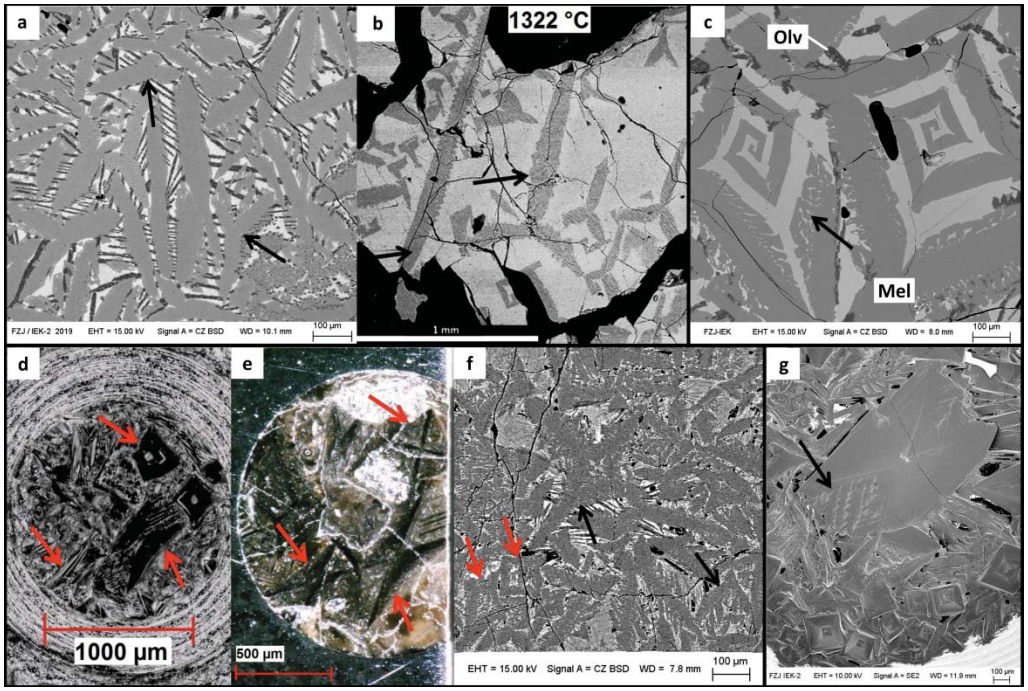

Fig. 13: Selection of melilite crystal shapes and morphologies. a SEM BSE image of a CLSM sample supercooled to 1100 °C and hold for 7 minutes. b SEM BSE image of a slag system, quenched under air at 1322 °C, modified after Schwitalla et al., 2017. c sample quenched instantly from 1150 °C in the quenching experiment. d microscope image of sample surface, e surface cross section, and f SEM BSE image of the vertical cross section of a sample supercooled with -200 K/min in the CLSM experiment. g SEM image of the sample surface, supercooled with -60 K/min in the CLSM experiment.

Melilite crystals displayed in Fig. 12 a, indicated Y- to skeletal crystal shapes. A similar shape was observed in a coal slag after viscosity measurements by Schwitalla et al., 2017 [15] (Fig. 12 b) for a melilite solid solution, also dominated by åkermanite. Due to the similar shapes, it can be suspected that there is an overall mechanism responsible for the melilite crystal shape formation. To complete the observed variations of melilite shapes, a quadrangular spiral shell structure was also observed (Fig. 12 c). To comprehend the connection of all described shapes, a representative CLSM sample was intensively analysed (Fig. 12 d-f). Microscopic analysis of the samples surface revealed elongated square pyramidal shaped melilite crystals, as indicated by the red arrows (Fig. 12 d). After sample preparation, those crystals appear in an hour-glass shape in the cross section of the sample (Fig. 12 e). Thus, a prepared

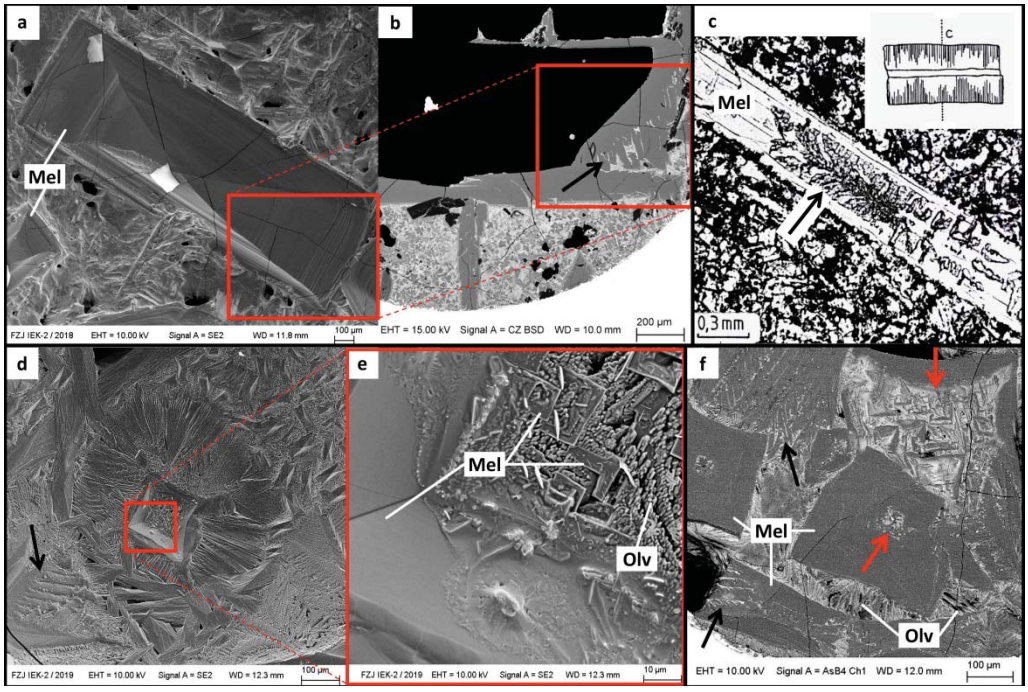

Fig. 14: SEM and SEM BSE images of the sample surface a and cross section b of an HKR sample, investigated in the CLSM experiment. c idiomorphic åkermanite crystal with a sketch of its inner peg-structure, modified after Pichler & Schmitt-Riegraf (1982). d, e SEM image of slag topography, sample supercooled with -150 K/min in the CLSM set up. f SEM image of supercooled slag (-200 K/min), investigated in the CLSM set up.

perpendicular cross section of the same sample showed the Y- shaped skeletal crystals again (Fig. 12 f, black arrows), while they were arranged with hollow melilite square crystals (red arrows). Based on these observations, it can be confirmed that pyramidal

melilite crystals and skeletal ones coexist next to each other. Furthermore, the inner structure of melilite pyramids is not completely filled, as the hour-glass shape of melilite pyramids in the cross section indicate.

The aforementioned observations can be enhanced by the analysis of the chosen slag samples, displayed in Fig. 13. An mm-scale, elongated melilite pyramid, which grew in the CLSM experiment at 1100 °C, was investigated (Fig. 13 a, b). Its outer

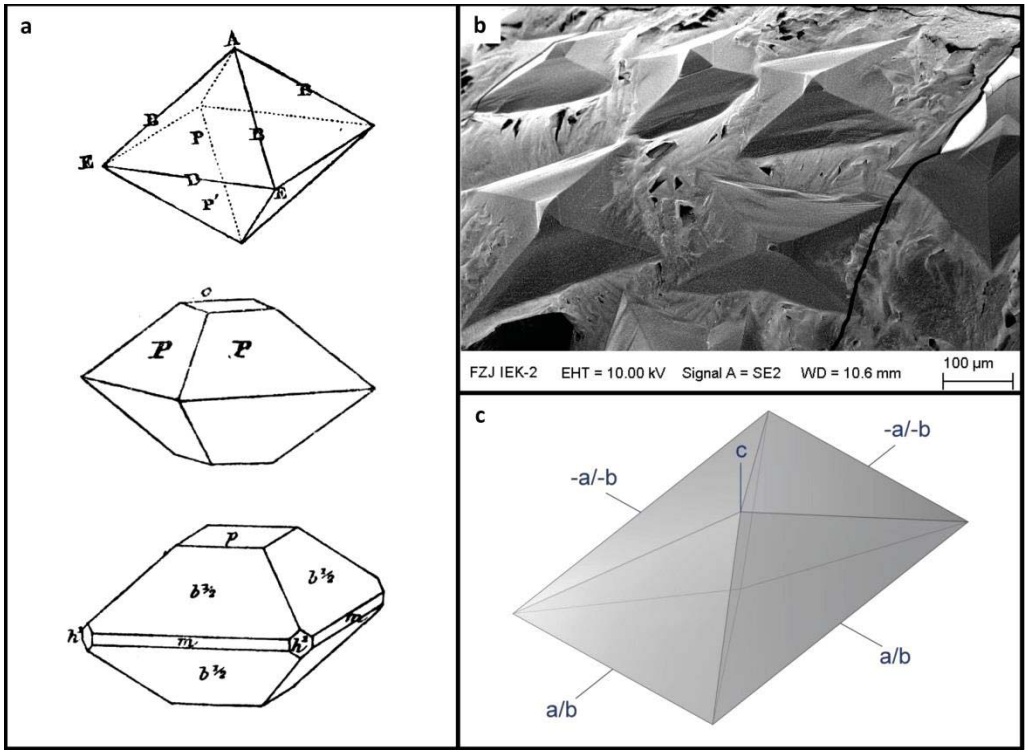

Fig. 15: a selection of melilite morphologies as already described by Goldschmidt (1920). b SEM image of sample morphology, sample treated in the CLSM experiment at 1200 °C for 60 minutes. c generalized rectangular bipyramid. The dimensions of the ground surface are described by the aspect ratio and its elevation in c-axis by a 35° angle of the face diagonal above the ground surface.

morphology is a distinctive pyramidal structure, with mainly smooth crystal surfaces that show signs of horizontal growth lamella. The analysed cross section of the pyramid revealed instead that it is partly hollow on the inside (Fig. 13 b, black arrow). Furthermore, the inner structure has a skeletal appearance, built up of an oblique main axis and smaller teeth-like outgrowths. Those structures align well with previous skeletal melilite structures (Figs. 4 a, 7 a, b, and 12 a, b, f). The frequent occurrence of the inner skeletal structures can be further legitimized by the åkermanite crystal, displayed in Fig. 13 c. The shown åkermanite crystal has a rectangular elongated

543 shape and is hollow on the inside accompanied by teeth-like outgrowths (Fig. 13 c).
544 The combination of its hollow nature with the internal outgrowths is described as the
545 “peg-structure” [37] and represents a special property of the melilite phase. Finally, it
546 can be summarised that the presence of skeletal melilite crystals in the cross sections
547 coincides with the rectangular pyramid structure as they are describing the same
548 crystal from different point of views (Figs. 4, 5, 7, and 12). Additionally, there is
549 further evidence for the hollow characteristic of melilite pyramid crystals. As already
550 visible in Fig. 12 f (red arrows) the cross section included some rectangular melilite
551 crystals, with a portion of remaining slag in its centre. Similar structure of melilite
552 pyramids is given in Fig. 13 d, e, and f. Supercooled HKR slag with an applied
553 supercooling rate of -150 K/min led to the formation of large melilite pyramids, whose
554 upper external morphology was not completed due to limited crystal growth
555 (Fig. 13 d, e). The inner space of the pyramid showed additional crystallisation of
556 small rectangular melilite crystals and olivine macro crystals, which crystallised out of
557 the remaining inner liquid slag. Furthermore, another CLSM sample also displayed
558 such crystallisation in the inner space of melilite pyramids (Fig. 13 f, red arrows). It
559 can be summarised, that the inner structure of melilite crystals has a complex growth
560 systematic, while its outer morphology displayed highly symmetric pyramids.
561 Since the characteristics of melilite pyramidal growth was intensively discussed, an
562 individual morphology was determined for its quantification. Fig. 14 a displayed a
563 selection of pyramidal melilite crystal morphologies [38], considering the restrictions
564 of melilite tetragonal crystallographic system. As the tetragonal crystallographic
565 system has a high degree of symmetries, the pyramidal habits are formed as
566 bipyramids. Due to the performed CLSM experiments melilite pyramids could only be
567 investigated from the top view (Fig. 14 b). It could not be validated, if the pyramidal
568 morphology turned out to be a bipyramidal one, since the bottom of the crystals was
569 submerged in the slag. However, as the symmetric restrictions of the tetragonal
570 crystallographic system could not be ignored, a bipyramidal melilite morphology is
571 the only reasonable generalisation, as seen in Fig. 14 b.

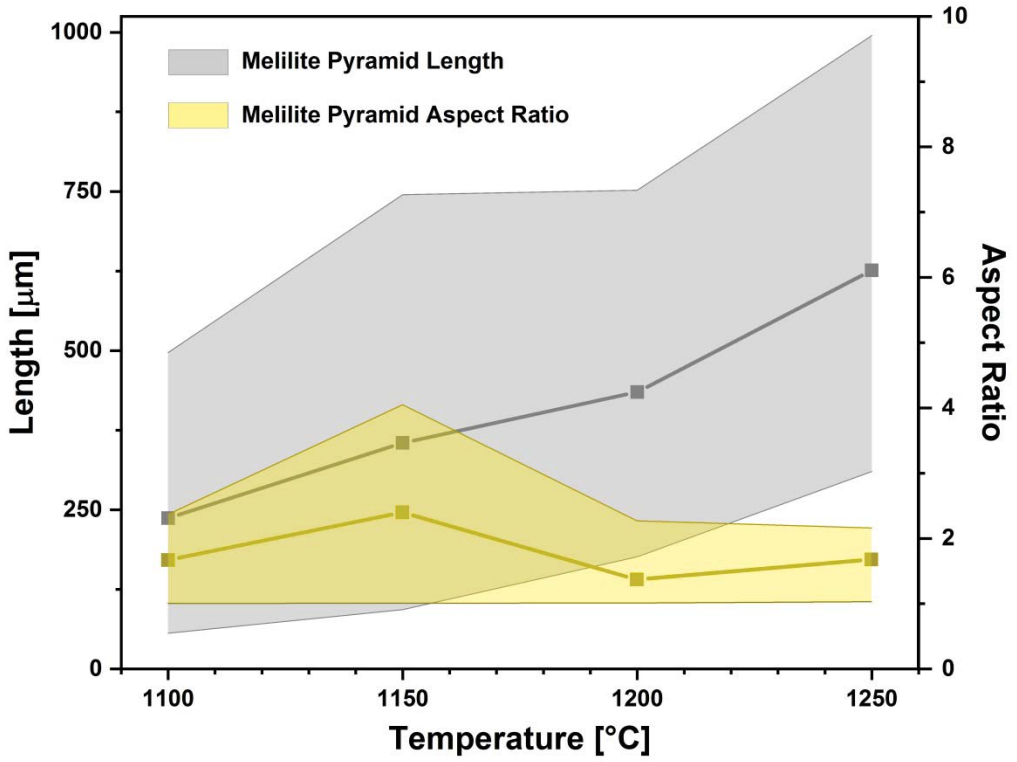

Fig. 16: Melilite crystal morphology quantification based on samples from the quenching and the CLSM experiments. 90th, 10th quantile, and average crystal length as well as melilite aspect ratio in dependency of the temperature.

572

573 Since the melilite crystal morphology was described, its dimensions were quantified.
574 A selection of 10 samples was chosen for the quantification, including two samples
575 from the quenching and eight samples from the CLSM experiments. Melilite pyramids
576 were measured based on digital microscopy and SEM images. In total, 83 melilite
577 pyramids were quantified on their length and on their aspect ratio, respectively. The
578 melilite quantification results are shown in Fig. 15. The average pyramid length is
579 increasing, as the degree of supercooling is reduced, a finding that was already
580 concluded for olivine (Fig. 11) and that is in agreement with the fundamentals of the
581 crystallisation theory [39]. To describe the span width of melilite length growth, the
582 10th and 90th quantile was chosen, since some individual large pyramids, e.g. the one
583 seen in Fig. 13 a and b, strongly impacted the maximum and minimum length value.
584 In contrast to the crystal length, the aspect ratio of melilite pyramids did not display a
585 specific trend. The highest average aspect ratio (2.4) of melilite pyramids was detected
586 at 1150 °C, all remaining temperature regimes led melilite crystals to grow in aspect
587 ratios between 1.37 (1200 °C) and 1.68 (1100 °C). A noteworthy finding is the fact

588 that the lowest determined aspect ratios were settled at around the value of 1, which
589 means that the melilite bipyramidal crystals had a square ground surface. In fact,
590 approx. 40 % of the quantified pyramids were in a square ground shape. Since no
591 systematic of elongated and square pyramids was found, the generalised elongated
592 bipyramidal structure was set to be ideal.
593
594

595 # 4 Conclusion

596 This study provided a new approach to ascertain crystallisation in partial liquid
597 gasifier slags. The generated data on the crystallised phases can be used as datasets
598 that can be implemented in a viscosity model for partially crystallised slags. The
599 crystallisation characteristics of the analysed, synthetic slag system were investigated
600 by thermochemical equilibrium calculations, quenching and CLSM experiments, and
601 subsequent analysis by XRD and SEM. Lastly, the advantages of the utilization of
602 crystal morphology data in a conceptual model were declared.
603 Thermochemical equilibrium calculations were performed using FactSage software
604 and GTox database. As a result, four phases were predicted to crystallise out the
605 supercooled slag system: melilite ($Ca_2(Al,Mg)(Si,Al)_2O_7$), olivine ($(Mg,Ca,Fe)_2SiO_4$),
606 spinel (AB_2O_4) and anorthite ($CaAl_2Si_2O_8$). Melilite, olivine and spinel were found in
607 the slag as crystallised phases, but anorthite was not present. Melilite and olivine were
608 detected by XRD analysis, in strong favour of melilite. Based on the CLSM and
609 quenching experiments, crystallisation kinetics indicated comparably short incubation
610 times and rapid crystallisation. The initial crystallisation temperature reduces, as the
611 cooling rate is increased. The temperature of crystallisation completion reduces
612 continuously with the increasing cooling rates.
613 The slag contained y-shaped, skeletal to pyramidal melilite macro crystals, followed
614 by rhomboid shaped smaller olivine crystals that tended to form elongated macro
615 crystals. The variety of melilite crystallisation forms could be explained by a hollow,
616 skeletal inner structure of the externally pyramids. Melilite crystals were generalised

as rectangular bipyramids and their length and aspect ratio were quantified. The aspect ratio underlies fluctuations around values of 1.4 and 2.4 while the bipyramidal length is increasing with a lower degree of supercooling. The olivine phase was generalised as an elongated, equiaxed bipyramid. Such morphology aligns very well with characteristic olivine crystals documented in the fields of mineralogy and crystallography. Its quantification also indicated larger crystals at higher temperatures. However, olivine aspect ratio is constant (2.13- 2.25) over the entire analysed temperature range, indicating that olivine crystals grow uniformly in shape.

A conceptual approach of a viscosity model for partially crystallised slags was stated. State of the art models include simplifications on the volume fraction of crystallised phases that are expected to be spherical. However, crystal phases occupy distinct morphologies, as proven in this study. As a result, specific maximum volume fractions can be ascertained for each individual crystallised phase. The usage of effective volume fractions, based on the individual crystal morphology, is the more valuable approach that should be realised in the future.

Acknowledgement

The work described in this paper has been performed in the framework of the HotVeGas Project supported by Bundesministerium für Wirtschaft und Energie (FKZ 0327773).

Literature

[1] P.K. Johne, P.; Fendt, S.; Spliethoff, H. , Fuel & Load-Flexible Entrained Flow Gasifier Operation & Applications: Flame Parameters & Flexible Burner in: 27th International Conference on the Impact of Fuel Quality on Power Production and the Environment, Lake Louise, Canada, 2018, pp. 13.

[2] M. Dohrn, M. Müller, Influence of Load Changes on the Deposit Behavior during Combustion of Five Different Hard Coals, Energy and fuels, 32 (2018) 3985-3994. https://doi.org/10.1021/acs.energyfuels.7b04020.

[3] S. Halama, H. Spliethoff, Numerical simulation of entrained flow gasification: Reaction kinetics and char structure evolution, Fuel Process. Technol., 138 (2015) 314-324. https://doi.org/10.1016/j.fuproc.2015.05.012.

[4] S. DeYoung, CFD simulations of an industrial scale entrained flow gasifier: Influence of gasifier design and operating conditions, in: 9th International Freiberg Conference on IGCC & XtL Technologies, Berlin, 2018, pp. 14.

[5] A. Funke, A. Niebel, D. Richter, M.M. Abbas, A.K. Müller, S. Radloff, M. Paneru, J. Maier, N. Dahmen, J. Sauer, Fast pyrolysis char – Assessment of alternative uses within the bioliq® concept, Bioresource Technology, 200 (2016) 905-913. https://doi.org/10.1016/j.biortech.2015.11.012.

[6] A. Mishra, S. Gautam, T. Sharma, Effect of operating parameters on coal gasification, International Journal of Coal Science & Technology, 5 (2018) 113-125. 10.1007/s40789-018-0196-3.

[7] S. Seebold, The influence of crystallization on the flow of coal ash-slags, Fuel, 187 (2017) 376-387. http://dx.doi.org/10.1016/j.fuel.2016.09.078.

[8] S. Seebold, M. Eberhard, G. Wu, E. Yazhenskikh, D. Sergeev, T. Kolb, M. Müller, Thermophysical and chemical properties of bioliq slags, Fuel, 197 (2017) 596-604. https://doi.org/10.1016/j.fuel.2017.02.027.

[9] G. Wu, E. Yazhenskikh, K. Hack, E. Wosch, M. Müller, Viscosity model for oxide melts relevant to fuel slags. Part 1: Pure oxides and binary systems in the system SiO2–Al2O3–CaO–MgO–Na2O–K2O, Fuel Process. Technol., 137 (2015) 93-103. http://dx.doi.org/10.1016/j.fuproc.2015.03.025.

[10] G. Wu, E. Yazhenskikh, K. Hack, M. Müller, Viscosity model for oxide melts relevant to fuel slags. Part 2: The system SiO2-Al2O3-CaO-MgO-Na2O-K2O, Fuel Process. Technol., 138 (2015) 520-533. https://doi.org/10.1016/j.fuproc.2015.06.031.

[11] C. He, J. Bai, L. Kong, J. Xu, S. Guhl, X. Li, Z. Ge, X. Cao, Z. Bai, W. Li, Effects of atmosphere on the oxidation state of iron and viscosity behavior of coal ash slag, Fuel, 243 (2019) 41-51. https://doi.org/10.1016/j.fuel.2019.01.020.

[12] C. He, J. Bai, W. Li, L. Kong, J. Xu, S. Guhl, X. Li, Z. Bai, W. Li, Iron transformation behavior in coal ash slag in the entrained flow gasifier and the application for Yanzhou coal, Fuel, 237 (2019) 851-859. https://doi.org/10.1016/j.fuel.2018.09.134.

[13] A. Strandberg, N. Skoglund, M. Thyrel, T.A. Lestander, M. Broström, R. Backman, Time-Resolved Study of Silicate Slag Formation During Combustion of Wheat Straw Pellets, Energy & Fuels, 33 (2019) 2308-2318. 10.1021/acs.energyfuels.8b04294.

[14] Y. Wei, H. Li, N. Yamada, A. Sato, Y. Ninomiya, K. Honma, T. Tanosaki, A microscopic study of the precipitation of metallic iron in slag from iron-rich coal during high temperature gasification, Fuel, 103 (2013) 101-110. https://doi.org/10.1016/j.fuel.2011.09.024.

[15] D.H. Schwitalla, A.M. Bronsch, M. Klinger, S. Guhl, B. Meyer, Analysis of solid phase formation and its impact on slag rheology, Fuel, 203 (2017) 932-941. dx.doi.org/10.1016/j.fuel.2017.04.092.

[16] L. Zhuangzhuang, P. Lieven, B. Bart, G. Muxing, Viscosity of Heterogeneous Silicate Melts: A Review, Metallurgical and Materials Transactions B, 49 (2018) 2469-2486. 10.1007/s11663-018-1374-9.

[17] L. Kong, J. Bai, Z. Bai, Z. Guo, W. Li, Improvement of ash flow properties of low-rank coal for entrained flow gasifier, Fuel, 120 (2014) 122-129. http://doi.org/10.1016/j.fuel.2013.12.001.

[18] Z. Shen, R. Li, Q. Liang, J. Xu, H. Liu, Effect of Cooling Process on the Generation and Growth of Crystals in Coal Slag, Energy & Fuels, 30 (2016) 5167-5173. https://doi.org/10.1021/acs.energyfuels.5b02625.
[19] W. Xuan, Qian Wangb, Jiansheng Zhangb, D. Xia, Influence of silica and alumina (SiO2+Al2O3) on crystallization characteristics of synthetic coal slags, Fuel, 189 (2017) 39-45. https://doi.org/10.1016/j.fuel.2016.10.081.
[20] H.P. Yuan, Q.F. Liang, X. Gong, Crystallization of Coal Ash Slags at High Temperatures and Effects on the Viscosity, Energy & Fuels, 26 (2012) 3717-3722. https://doi.org/10.1021/ef201894p.
[21] Q. Ren, Y. Zhang, Y. Long, Z. Zou, J. Pei, Crystallisation behaviour of blast furnace slag modified by adding fly ash, Ceramics International, 44 (2018) 11628-11634. https://doi.org/10.1016/j.ceramint.2018.03.237.
[22] T. Melchior, Untersuchungen zur Oberflächenspannung von Kohleschlacken unter Vergaserbedingungen, in: Fakultät für Maschinenwesen, Rheinisch-Westfälische Technische Hochschule, Aachen, 2010, pp. 270.
[23] A. Schlüter, Untersuchungen zum Verschmutzungsverhalten rheinischer Braunkohlen in Kohledampferzeugern, in: Fakultät für Maschinenwesen (Fak. 4), Rheinisch-Westfäliche Technische Hochschule Aachen, Aachen, 2018, pp. 164.
[24] J.P. Schupsky, M. Guo, M. Müller, Investigations on Crystallisation Processes of Three Oxidic Gasifier Slag Systems, in: B.A. Sakkestad (Ed.) 44TH International Technical Conference on Clean Energy, Coal Technologies Associates, Clearwater, Florida, 2019, pp. 253-265.
[25] J.P. Schupsky, M. Guo, B. Blanpain, M. Müller, INFLUENCE OF PARAMETERS ON THE CRYSTALLISATION BEHAVIOUR OF OXIDIC SLAG SYSTEMS DETERMINED BY CLSM INVESTIGATIONS, in: P.A. Malfliet A., Di Maria A. (Ed.) 6th International Slag Valorisation Symposium, KU Leuven, Mechelen, Belgium, 2019,
[26] C.W. Bale, E. Bélisle, P. Chartrand, S.A. Decterov, G. Eriksson, A.E. Gheribi, K. Hack, I.H. Jung, Y.B. Kang, J. Melançon, A.D. Pelton, S. Petersen, C. Robelin, J. Sangster, P. Spencer, M.A. Van Ende, FactSage thermochemical software and databases, 2010–2016, Calphad, 54 (2016) 35-53. https://doi.org/10.1016/j.calphad.2016.05.002.
[27] T.J. K. Hack, M. Müller, E. Yazhenskikh, G. Wu, A novel thermodynamic database for slag systems and refractory materials, in: Proceedings of the 5th International Congress on the Science and Technology of Steelmaking, Dresden, Germany, 2012,
[28] W.W. Xuan, K.J. Whitty, Q.L. Guan, D.P. Bi, Z.H. Zhan, J.S. Zhang, Influence of Fe2O3 and Atmosphere on Crystallization Characteristics of Synthetic Coal Slags, Energy & Fuels, 29 (2015) 405-412. https://doi.org/10.1021/ef5020633.
[29] C.R. Brugger, J.E. Hammer, Crystal size distribution analysis of plagioclase in experimentally decompressed hydrous rhyodacite magma, Earth and Planetary Science Letters, 300 (2010) 246-254. https://doi.org/10.1016/j.epsl.2010.09.046.
[30] P.T. Jones, D. Desmet, M. Guo, D. Durinck, F. Verhaeghe, J. Van Dyck, J. Liu, B. Blanpain, P. Wollants, Using confocal scanning laser microscopy for the in situ study of high-temperature behaviour of complex ceramic materials, Journal of the European Ceramic Society, 27 (2007) 3497-3507. https://doi.org/10.1016/j.jeurceramsoc.2007.01.022.
[31] L. Zhuangzhuang, C. Liugang, M. Guo, B. Blanpain, Effect of Crystallization on the Abrupt Viscosity Increase during the Slag Cooling Process, ISIJ Int., 58 (2018) 1972-1978. https://doi.org/10.2355/isijinternational.ISIJINT-2018-176.
[32] G. Wu, Modelling and Experimental Validation of the Viscosity of Liquid Phases in Oxide Systems Relevant to Fuel Slags, in: Fakultät für Maschinenwesen, Rheinisch-Westfälische Technische Hochschule Aachen, Aachen, 2015,
[33] G. Wu, S. Seebold, E. Yazhenskikh, J. Tanner, K. Hack, M. Müller, Slag mobility in entrained flow gasifiers optimized using a new reliable viscosity model of iron oxide-containing multicomponent melts, Applied Energy, 236 (2019) 837-849. https://doi.org/10.1016/j.apenergy.2018.11.100.

[34] R. Roscoe, The viscosity of suspensions of rigid spheres, Br. J. Appl. Phys., 3 (1952) 267–269.
[35] I.M. Krieger, T.J. Dougherty, A Mechanism for Non-Newtonian Flow in Suspensions of Rigid Spheres, Trans. Soc. Rheol., 3 (1959) 137–152.
[36] W. Xuan, J. Zhang, D. Xia, The influence of MgO on the crystallization characteristics of synthetic coal slags, Fuel, 222 (2018) 523-528. https://doi.org/10.1016/j.fuel.2018.02.197.
[37] H. Pichler, C. Schmitt-Riegraf, Gesteinsbildende Minerale im Dünnschliff : 22 Tab, Ferdinand Enke Verlag, Stuttgart, 1987.
[38] V. Goldschmidt, Atlas der Krystallformen, Winter, Heidelberg, 1920.
[39] J. Liebertz, Crystal growth from melts of high viscosity, Progress in Crystal Growth and Characterization, 6 (1983) 361-369. https://doi.org/10.1016/0146-3535(83)90013-8.
[40] G. Tammann, Kristallisieren und Schmelzen: ein Beitrag zur Lehre der Änderungen des Aggregatzustandes, Kristallisieren und Schmelzen: ein Beitrag zur Lehre der Änderungen des Aggregatzustandes, (1903)

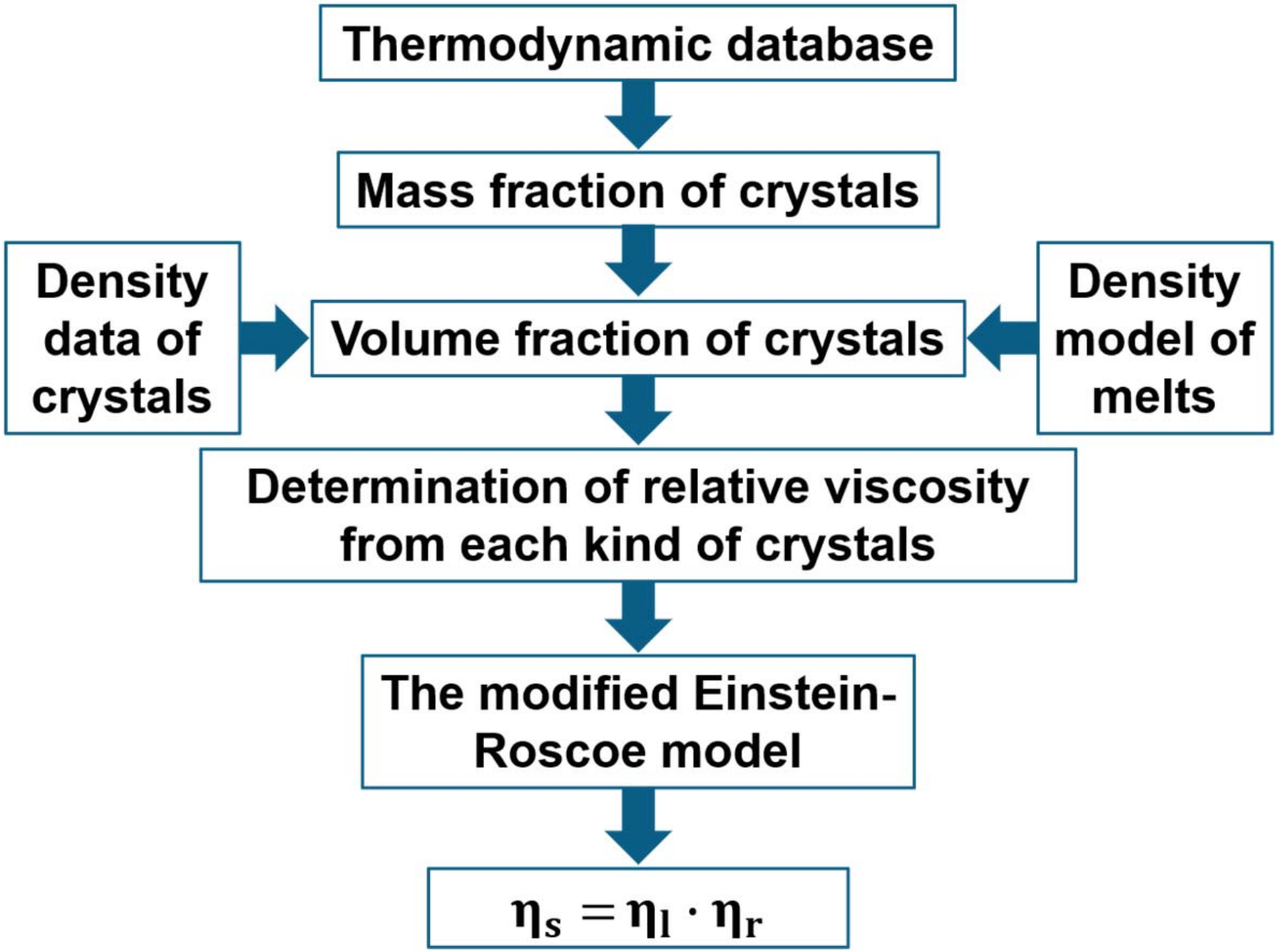
Thermodynamic database
Mass fraction of crystals
Density data of crystals
Volume fraction of crystals
Density model of melts
Determination of relative viscosity from each kind of crystals
The modified Einstein-Roscoe model
$\eta_s = \eta_l \cdot \eta_r$

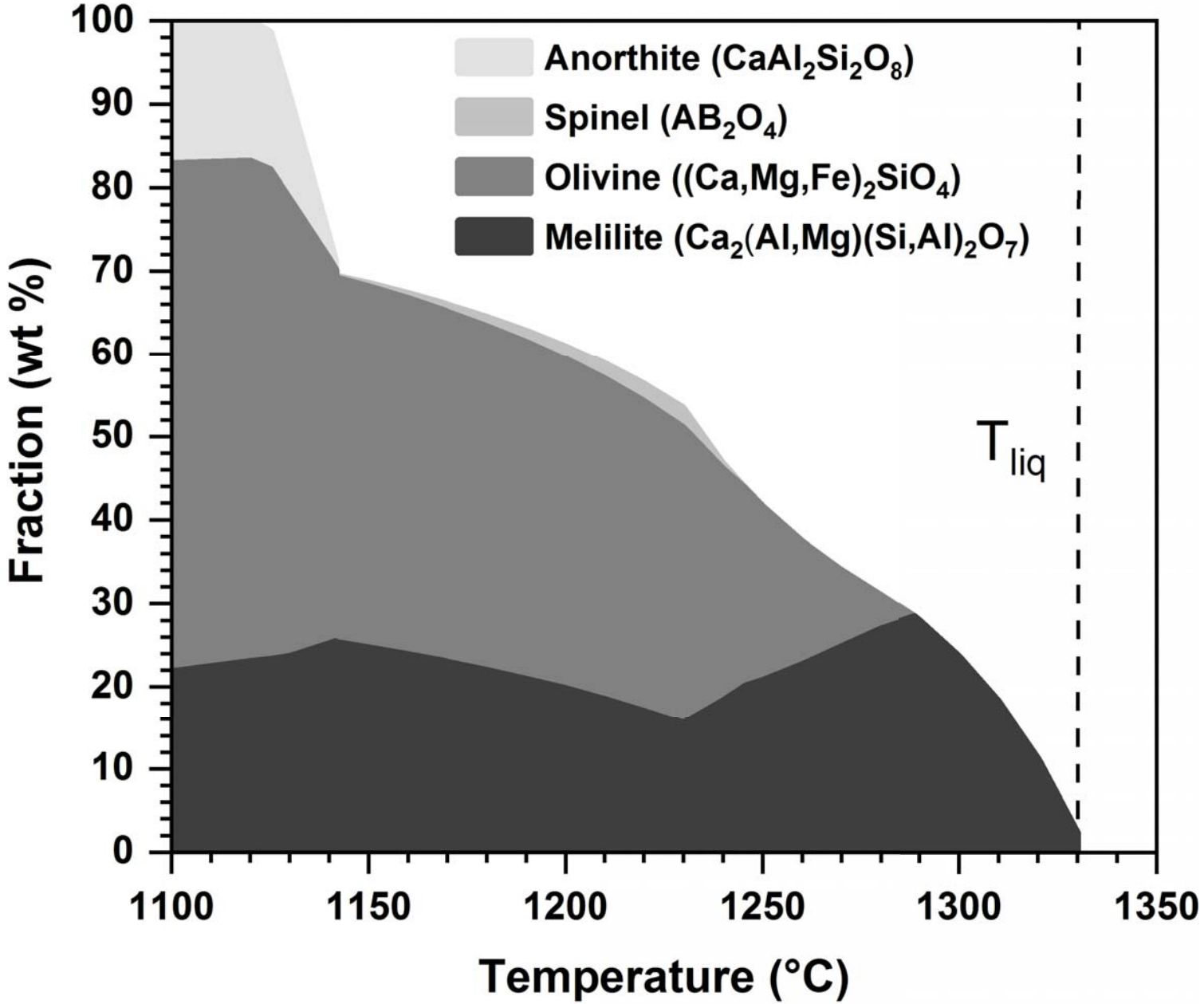
Anorthite ($CaAl_2Si_2O_8$)
Spinel (AB_2O_4)
Olivine ($(Ca,Mg,Fe)_2SiO_4$)
Melilite ($Ca_2(Al,Mg)(Si,Al)_2O_7$)
T_{liq}
Fraction (wt %)
Temperature (°C)
100
90
80
70
60
50
40
30
20
10
0
1100
1150
1200
1250
1300
1350

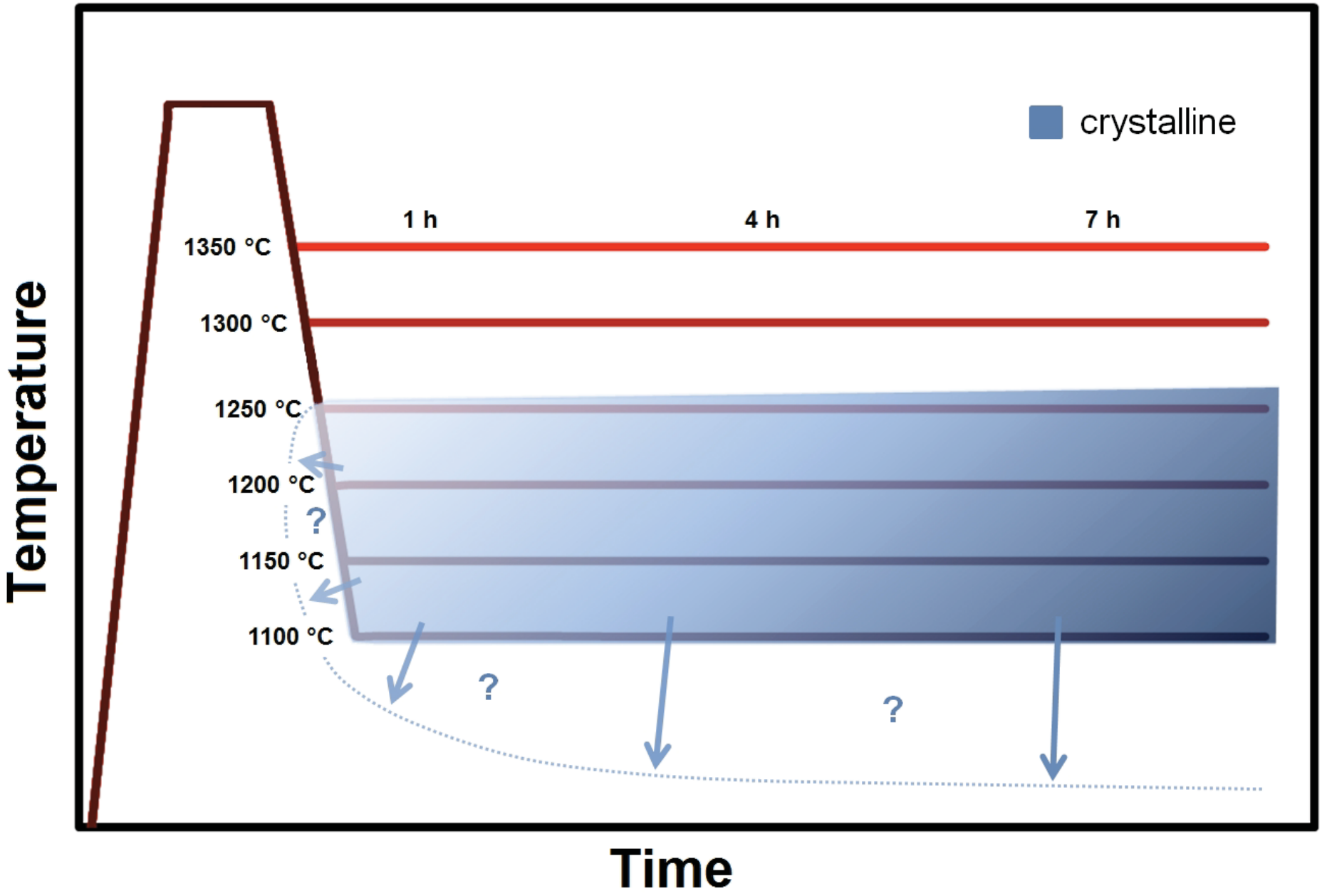
crystalline
1 h
4 h
7 h
1350 °C
1300 °C
1250 °C
1200 °C
?
1150 °C
1100 °C
?
?
Temperature
Time

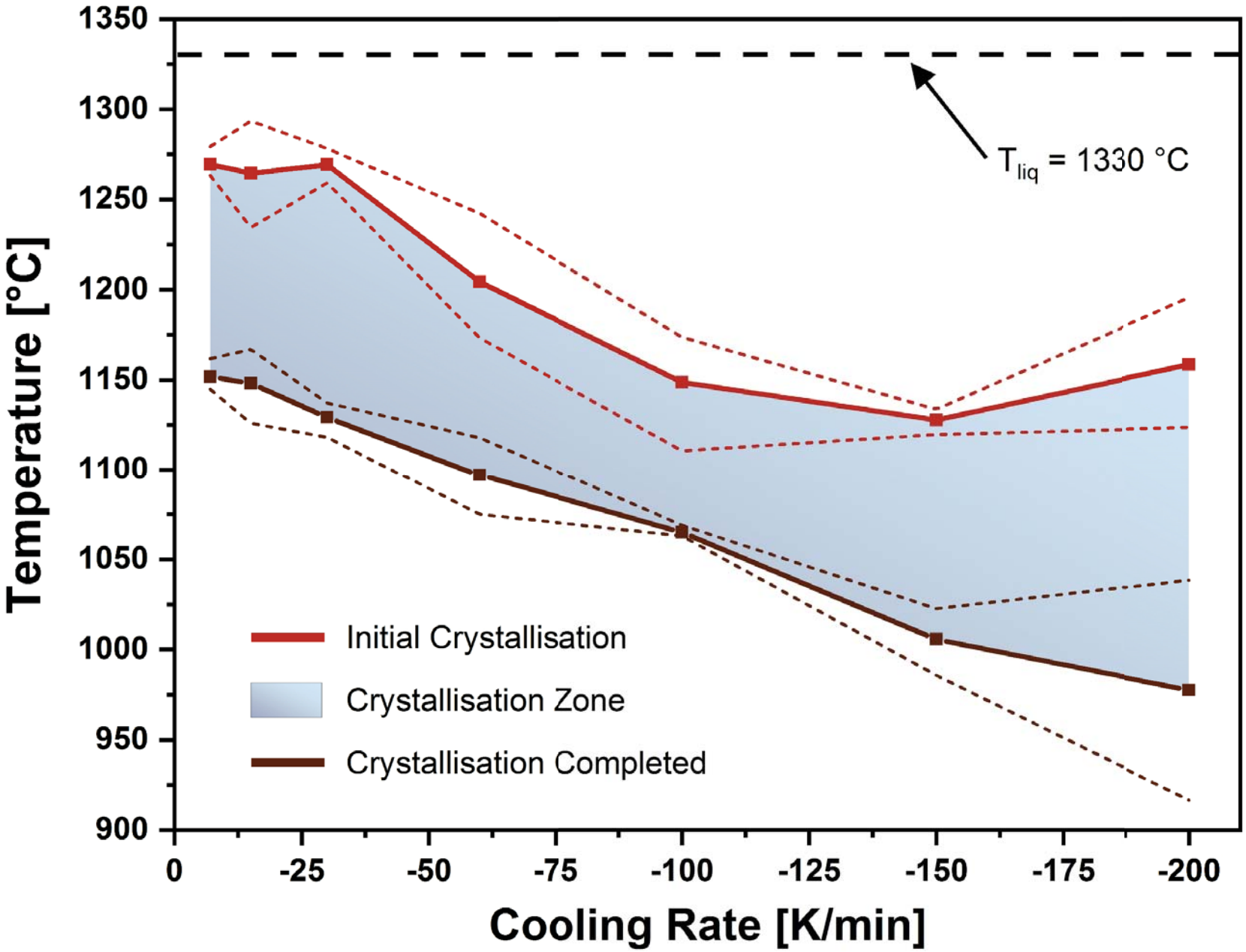
1350
1300
1250
1200
1150
1100
1050
1000
950
900
Temperature [°C]
0
-25
-50
-75
-100
-125
-150
-175
-200
Cooling Rate [K/min]
T_liq = 1330 °C
Initial Crystallisation
Crystallisation Zone
Crystallisation Completed

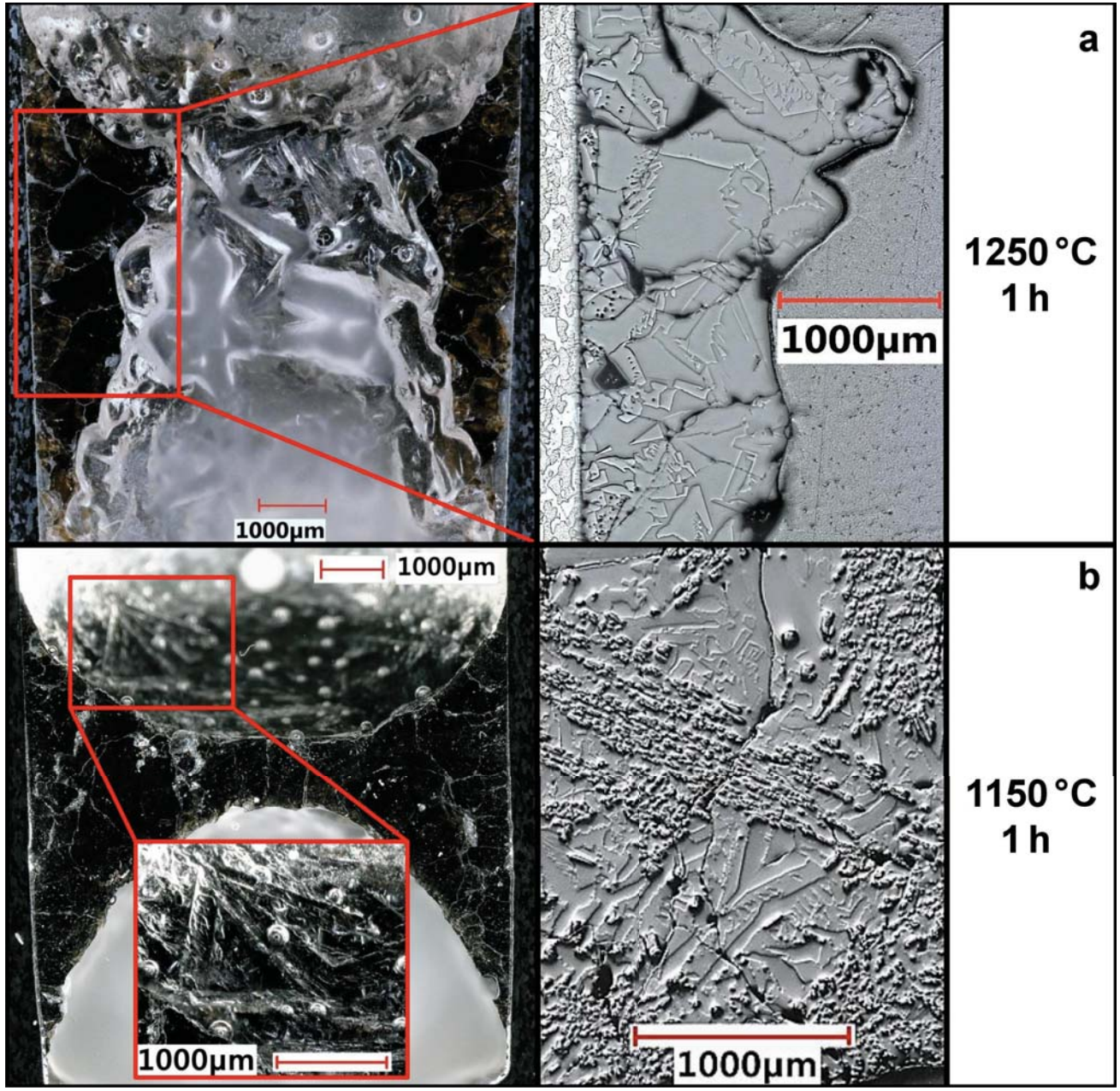
a
1250 °C
1 h
1000µm
1000µm
b
1150 °C
1 h
1000µm
1000µm

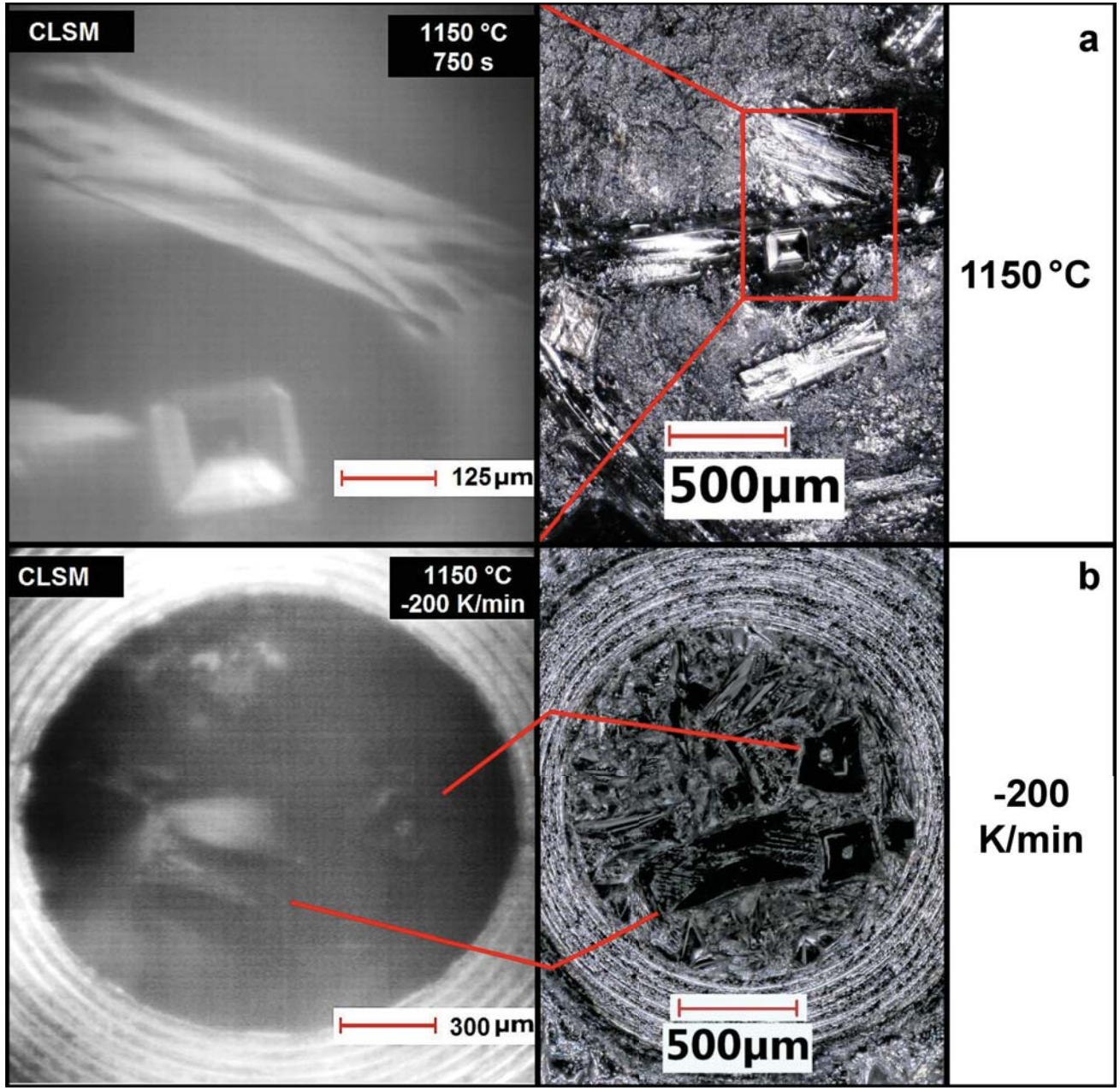
CLSM
1150 °C
750 s
125µm
500µm
a
1150 °C
CLSM
1150 °C
-200 K/min
300 µm
500µm
b
-200
K/min

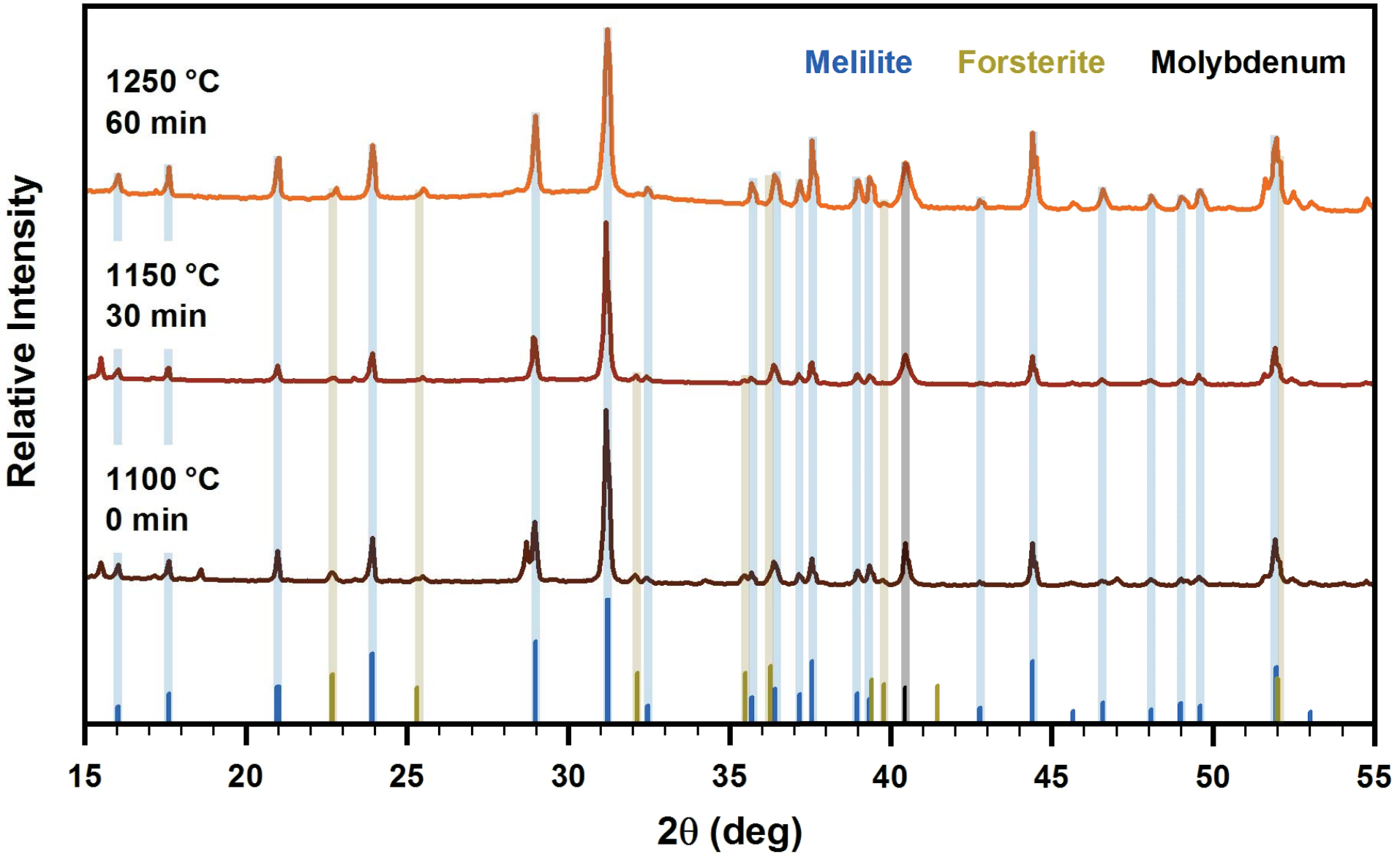
Melilite
Forsterite
Molybdenum
1250 °C
60 min
1150 °C
30 min
1100 °C
0 min
Relative Intensity
15
20
25
30
35
40
45
50
55
2θ (deg)

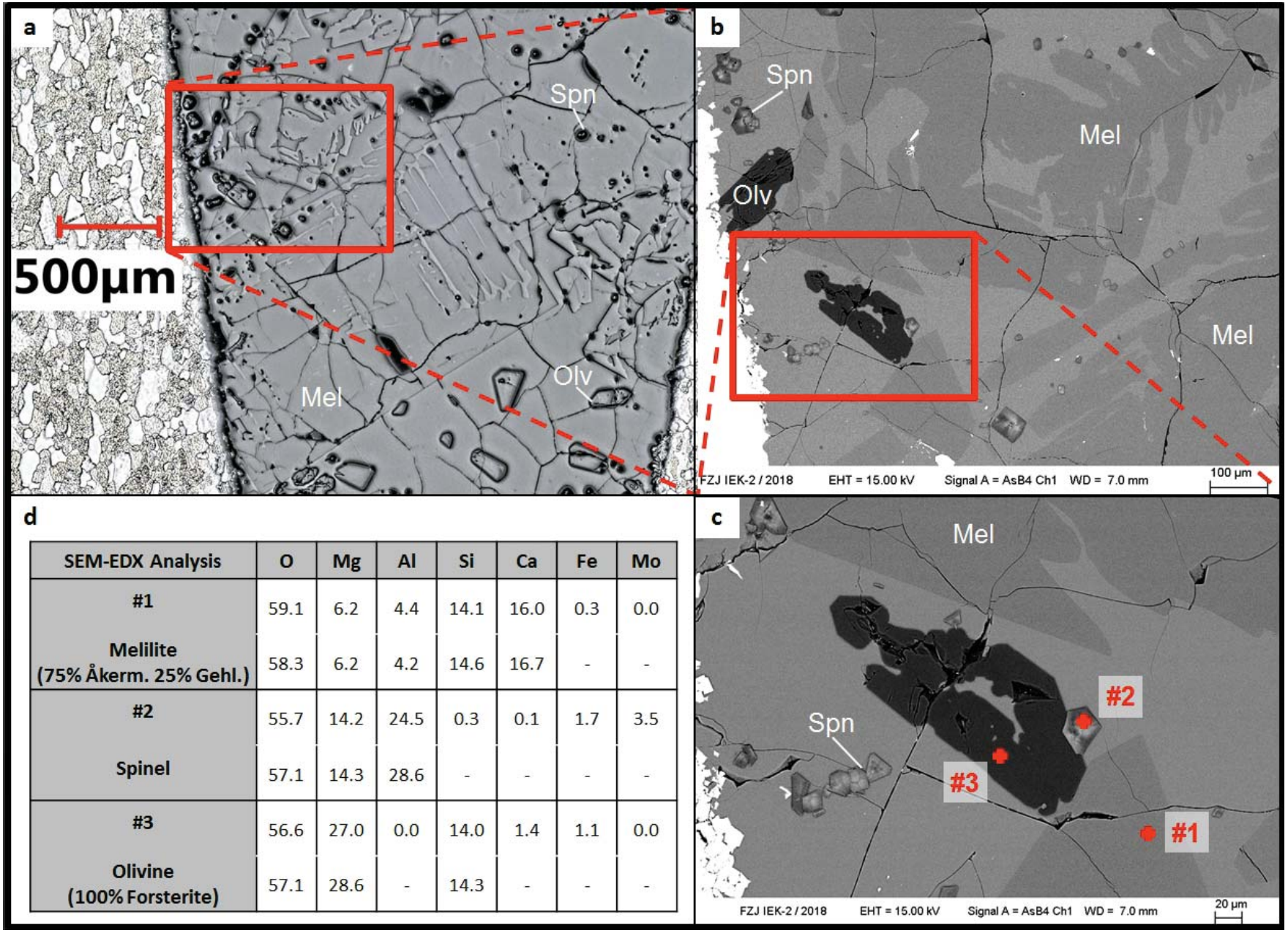

d

SEM-EDX Analysis	O	Mg	Al	Si	Ca	Fe	Mo
#1	59.1	6.2	4.4	14.1	16.0	0.3	0.0
Melilite (75% Åkerm. 25% Gehl.)	58.3	6.2	4.2	14.6	16.7	-	-
#2	55.7	14.2	24.5	0.3	0.1	1.7	3.5
Spinel	57.1	14.3	28.6	-	-	-	-
#3	56.6	27.0	0.0	14.0	1.4	1.1	0.0
Olivine (100% Forsterite)	57.1	28.6	-	14.3	-	-	-

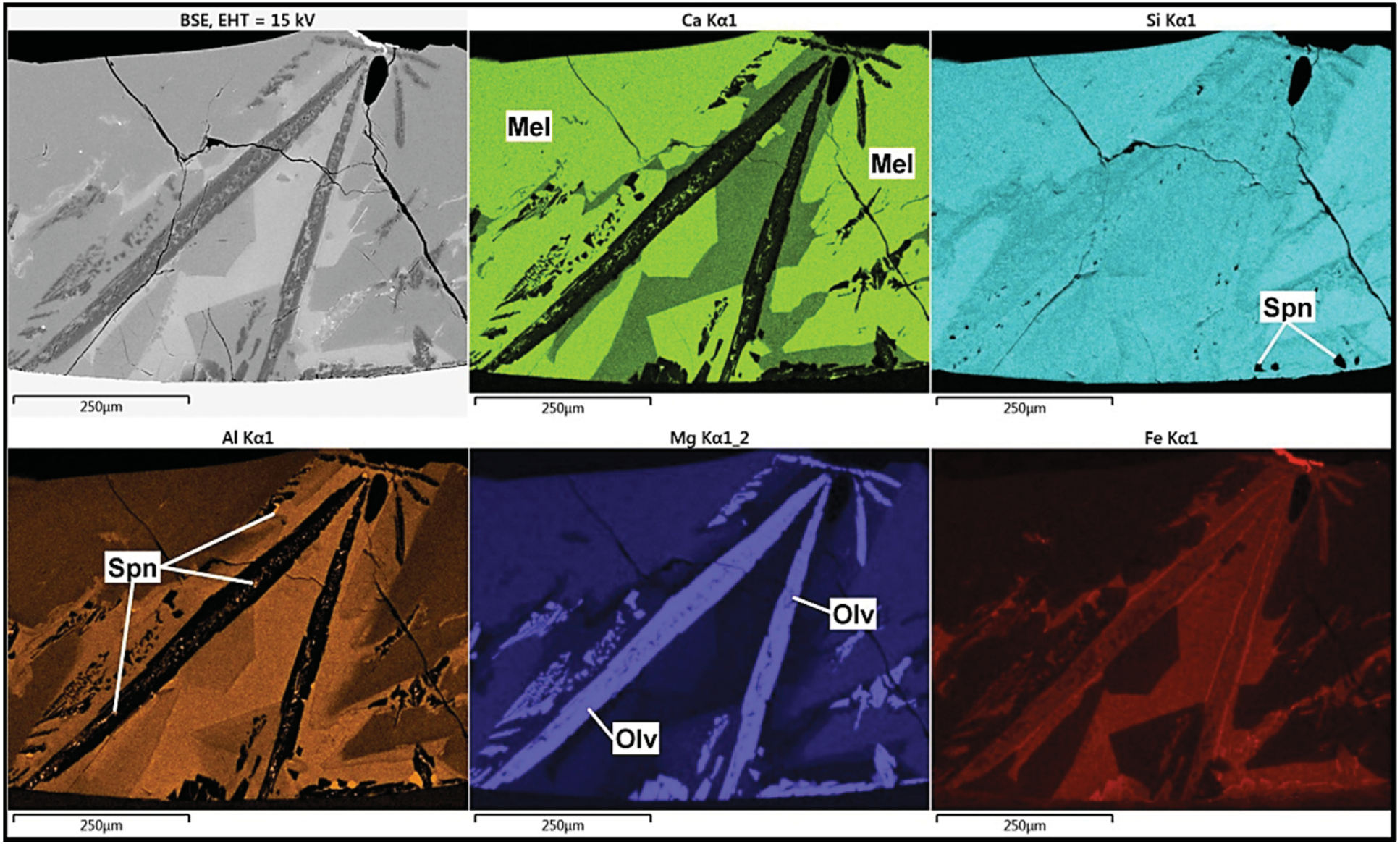
BSE, EHT = 15 kV
Ca Kα1
Si Kα1
Mel
Mel
Spn
250µm
250µm
250µm
Al Kα1
Mg Kα1_2
Fe Kα1
Spn
Olv
Olv
250µm
250µm
250µm

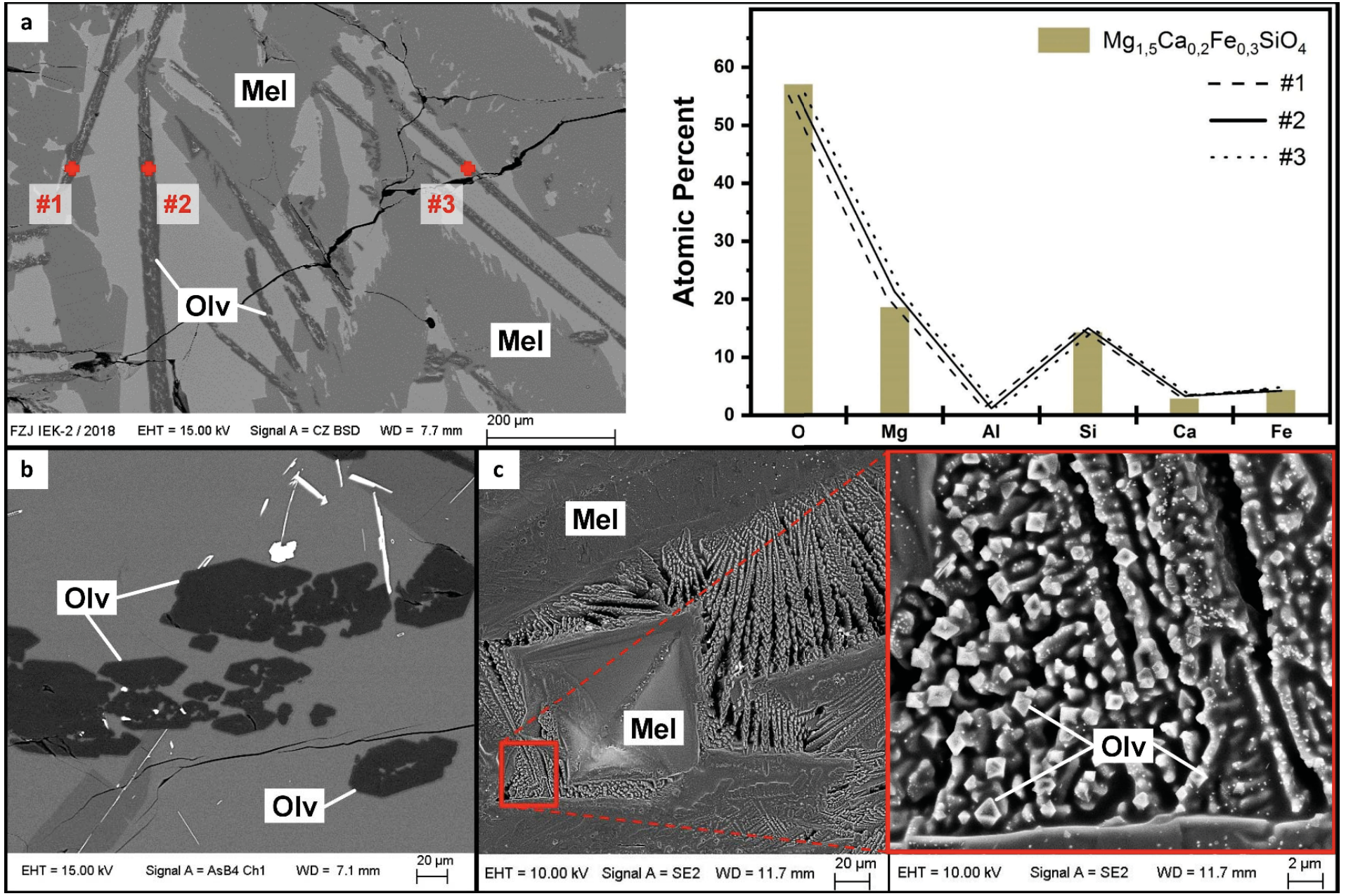
a
Mel
#1
#2
#3
Olv
Mel
FZJ IEK-2 / 2018 EHT = 15.00 kV Signal A = CZ BSD WD = 7.7 mm
200 µm
Mg1,5Ca0,2Fe0,3SiO4
#1
#2
#3
Atomic Percent
0
10
20
30
40
50
60
O
Mg
Al
Si
Ca
Fe
b
Olv
Olv
EHT = 15.00 kV Signal A = AsB4 Ch1 WD = 7.1 mm
20 µm
c
Mel
Mel
EHT = 10.00 kV Signal A = SE2 WD = 11.7 mm
20 µm
Olv
EHT = 10.00 kV Signal A = SE2 WD = 11.7 mm
2 µm

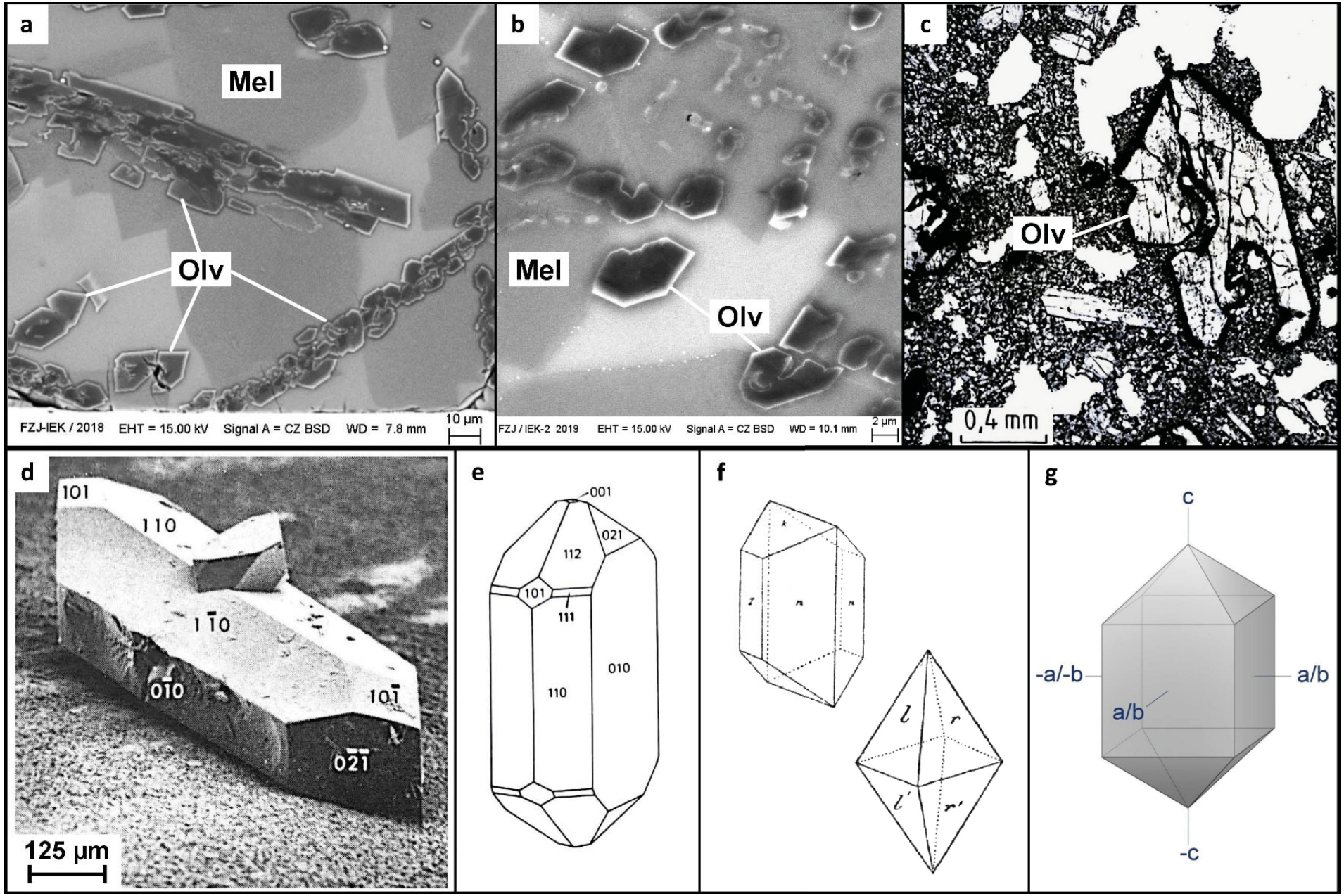
a
Mel
Olv
FZJ-IEK / 2018 EHT = 15.00 kV Signal A = CZ BSD WD = 7.8 mm
10 µm
b
Mel
Olv
FZJ / IEK-2 2019 EHT = 15.00 kV Signal A = CZ BSD WD = 10.1 mm
2 µm
c
Olv
0,4 mm
d
101
110
1 1̄0
01̄0
101̄
02̄1̄
125 µm
e
001
021
112
101
111
010
110
f
g
c
-a/-b
a/b
a/b
-c

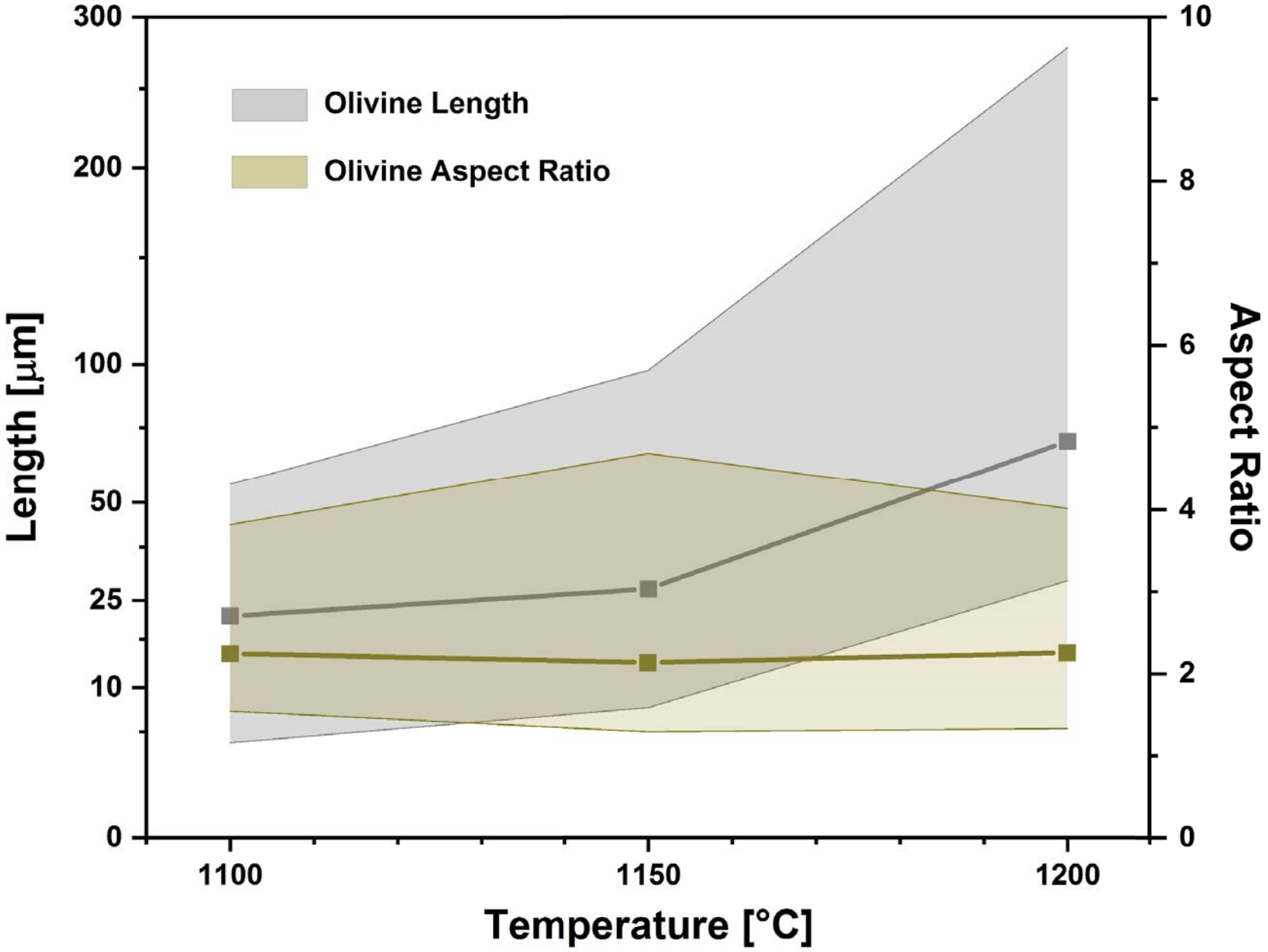
Olivine Length
Olivine Aspect Ratio
Length [μm]
Aspect Ratio
Temperature [°C]
300
200
100
50
25
10
0
10
8
6
4
2
0
1100
1150
1200

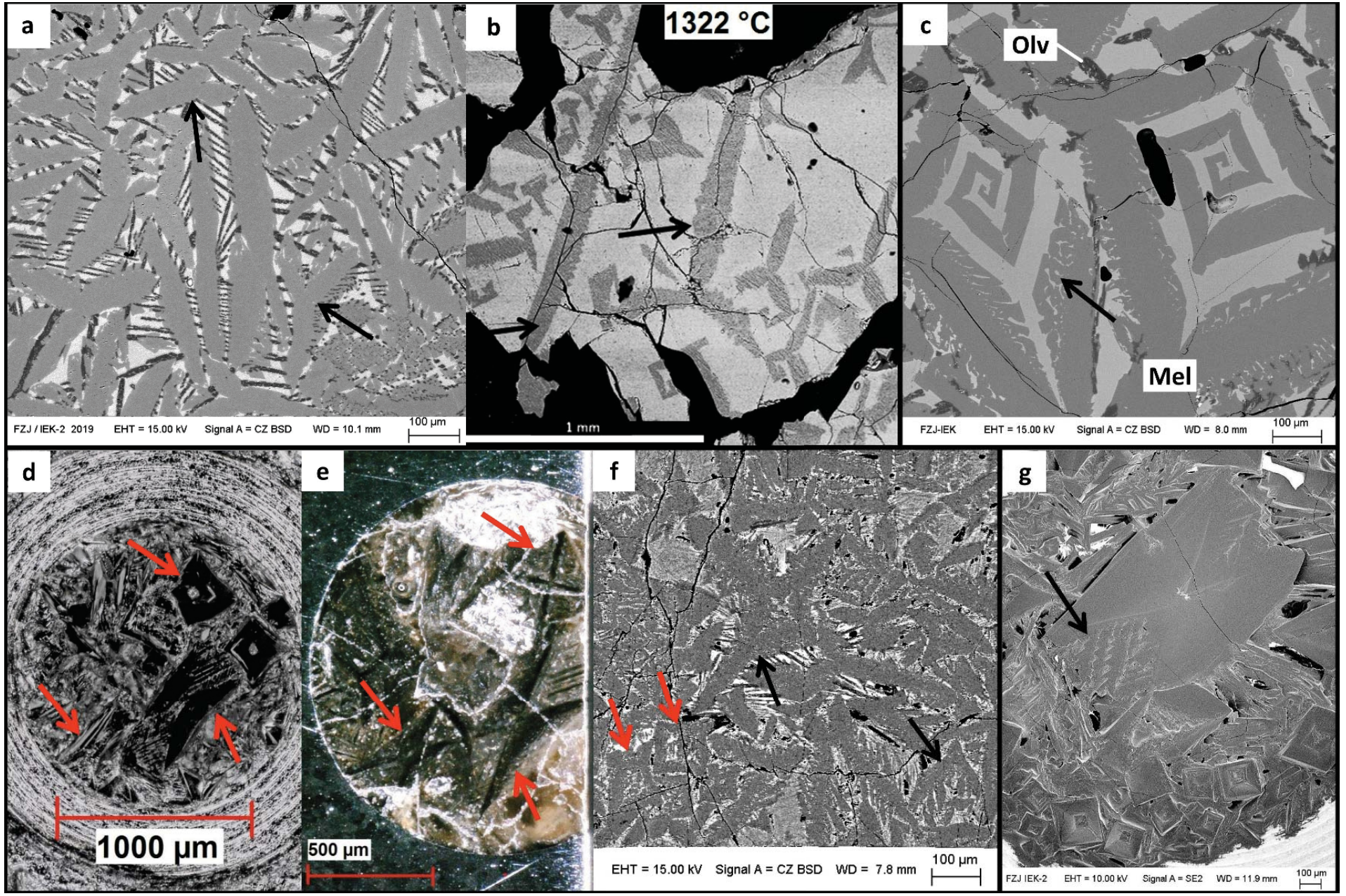
a
FZJ / IEK-2 2019 EHT = 15.00 kV Signal A = CZ BSD WD = 10.1 mm 100 µm
b
1322 °C
1 mm
c
Olv
Mel
FZJ-IEK EHT = 15.00 kV Signal A = CZ BSD WD = 8.0 mm 100 µm
d
1000 µm
e
500 µm
f
EHT = 15.00 kV Signal A = CZ BSD WD = 7.8 mm 100 µm
g
FZJ IEK-2 EHT = 10.00 kV Signal A = SE2 WD = 11.9 mm 100 µm

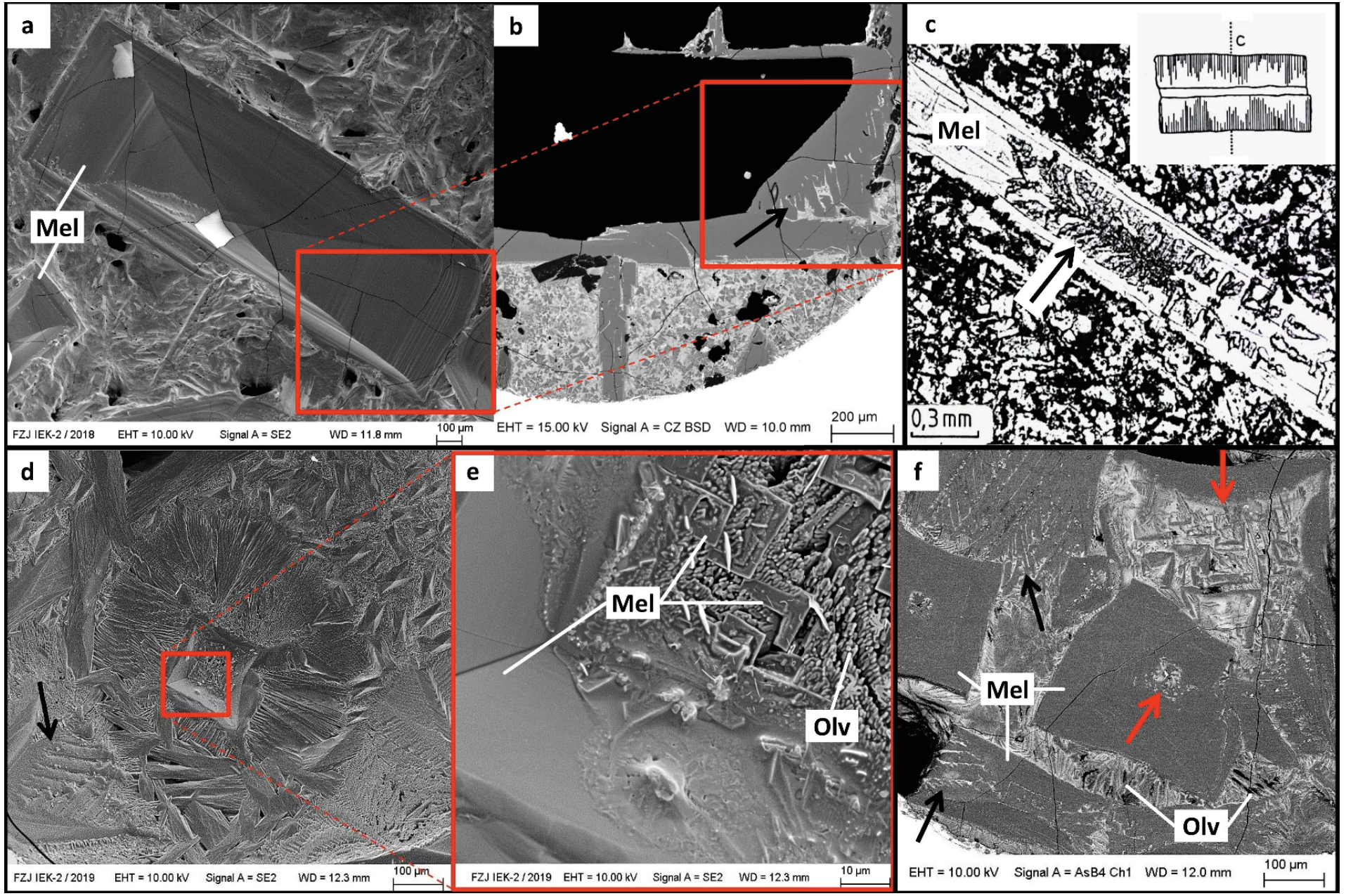
a
Mel
FZJ IEK-2 / 2018 EHT = 10.00 kV Signal A = SE2 WD = 11.8 mm 100 µm
b
EHT = 15.00 kV Signal A = CZ BSD WD = 10.0 mm 200 µm
c
Mel
c
0,3 mm
d
FZJ IEK-2 / 2019 EHT = 10.00 kV Signal A = SE2 WD = 12.3 mm 100 µm
e
Mel
Olv
FZJ IEK-2 / 2019 EHT = 10.00 kV Signal A = SE2 WD = 12.3 mm 10 µm
f
Mel
Olv
EHT = 10.00 kV Signal A = AsB4 Ch1 WD = 12.0 mm 100 µm

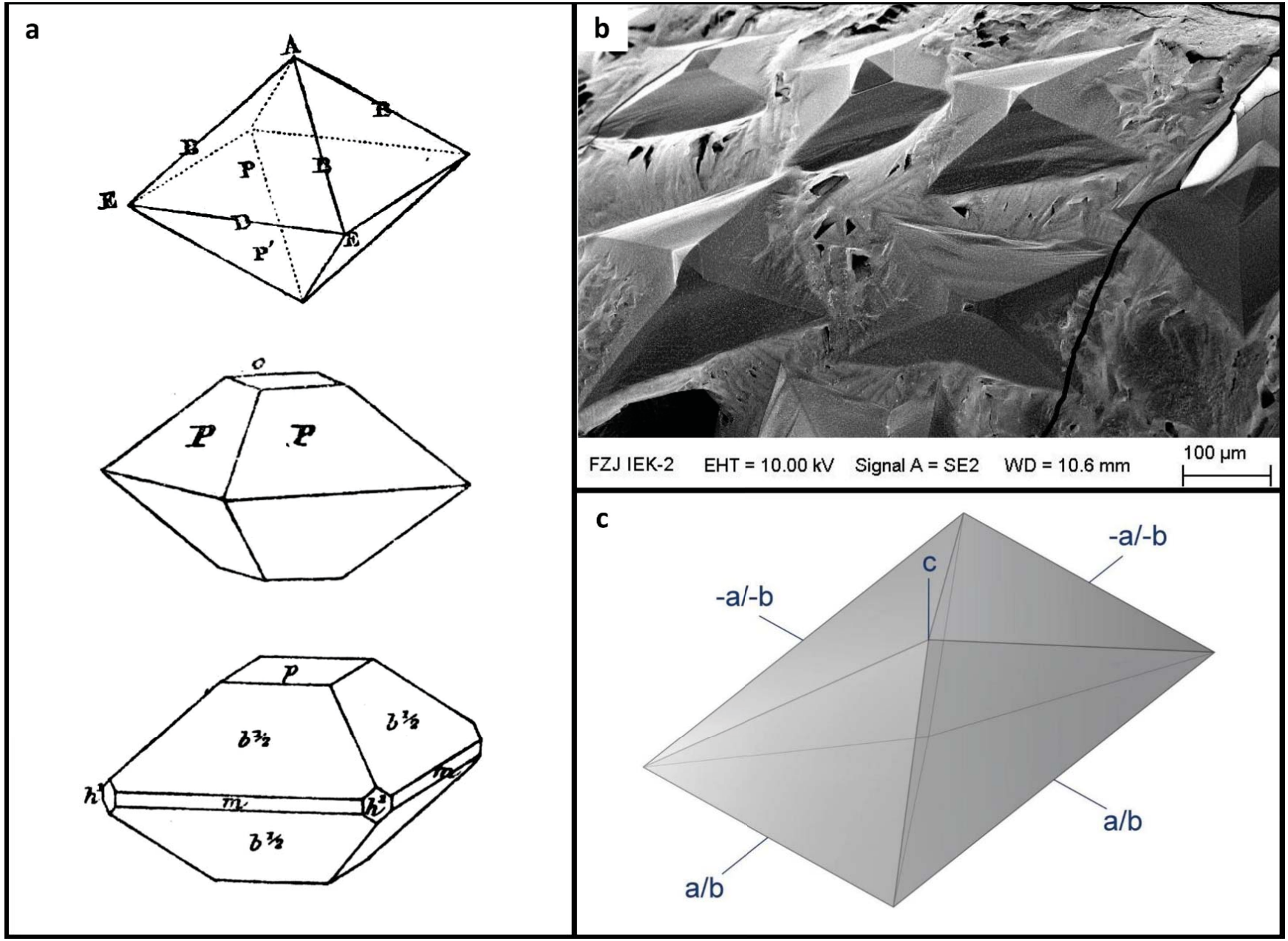
a
A
B
B
P
B
E
D
P'
E
o
P
P
p
b 3/2
b 3/2
h 1
m
h 2
b 3/2
b
FZJ IEK-2
EHT = 10.00 kV
Signal A = SE2
WD = 10.6 mm
100 µm
c
-a/-b
c
-a/-b
a/b
a/b

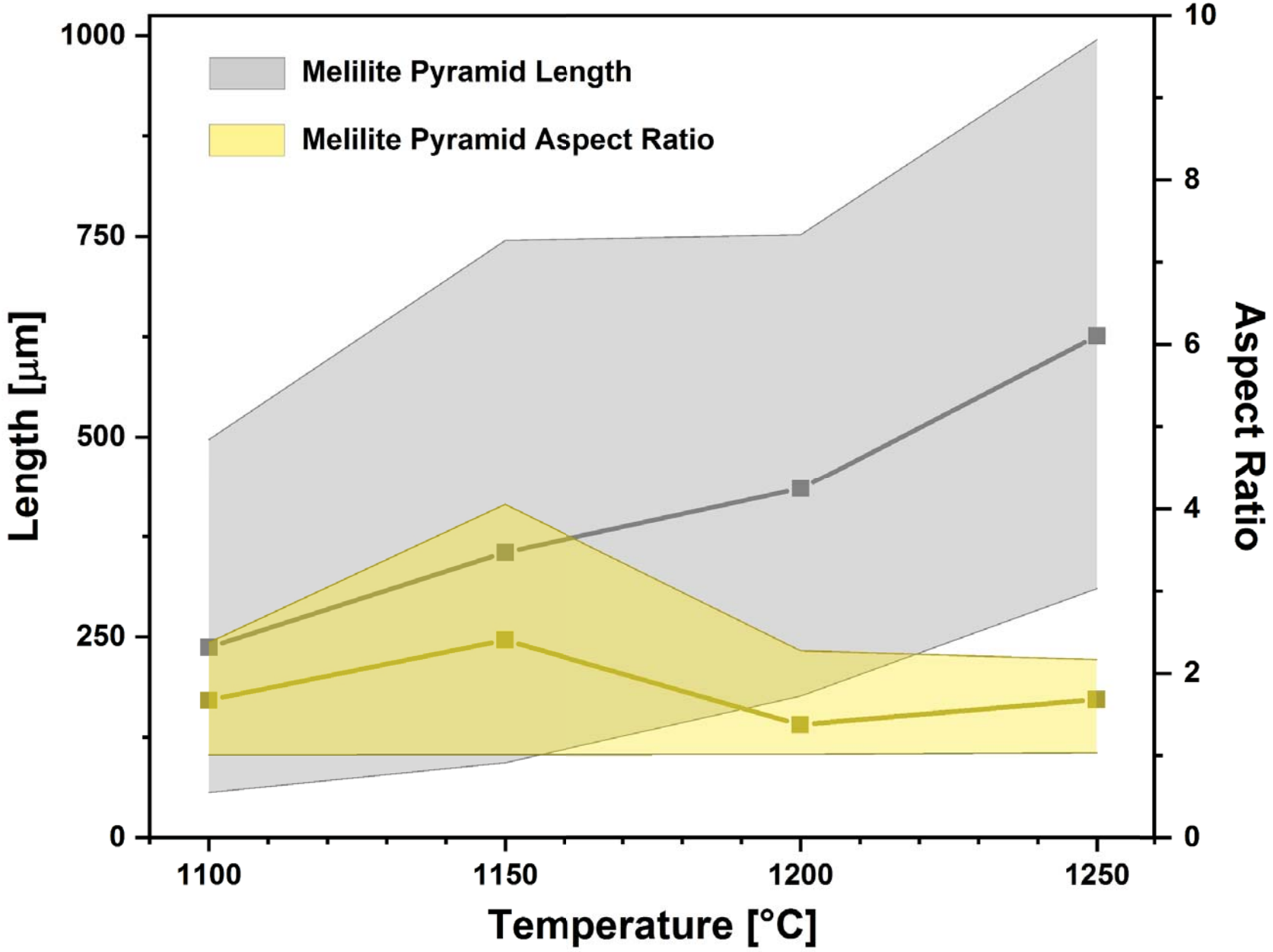
Melilite Pyramid Length
Melilite Pyramid Aspect Ratio
Length [μm]
Aspect Ratio
Temperature [°C]
1000
750
500
250
0
10
8
6
4
2
0
1100
1150
1200
1250

Table 1: Overview of the investigated crystal bearing slag systems by different authors. Crystal phases that are also covered in this study are underlined.

Author	Coal sample	Calculated crystal phases (FactSage)	Investigated crystal phases
Kong et al., 2014 [17]	YL (Yinli) GP (Gaoping) 50/50 blending	mullite, anorthite, cordierite, quartz, clinopyroxene	anorthite
Schwitalla et al., 2017 [15]	slag 3	melilite (>1300°C)	melilite (>1300°C)
Shen et al., 2016 [18]	chinese bituminous coal	hematite, anorthite andradite, gehlenite (melilite), melilite	gehlenite (melilite)
Xuan et al., 2017 [19]	synthetic slag #5	spinel, melilite, merwinite, Ca_2SiO_4	åkermanite (melilite), Mg-Fe-spinel, merwinite
Yuan et al., 2012 [20]	Shenfu	anorthite, wollastonite, gehlenite (melilite), melilite, Fe-spinel, wustite	anorthite, wollastonite, iron silicon oxide
Ren et al., 2018 [21]	BF slag with fly ash F - 2	melilite, anorthite, clinopyroxene, spinel	Åkermanite, gehlenite (melilite), clinopyroxene, anorthite

Table 2: Comparison of normalised HKR ash composition after combustion at 450 °C [22] with synthetic HKR slag used in this study. Both samples were analysed by ICP-OES and subsequently normalised to the oxidic compounds.

		SiO_2	Al_2O_3	CaO	MgO	Fe_2O_3	other
real HKR [22]	wt%	31.7	9.7	28.1	11.3	14.2	5.0
synthetic HKR	wt%	34.8	12.0	27.4	11.4	14.4	-